ACS APPLIED NANO MATERIALS

Article

Light-Confining Nanoporous Anodic Alumina Microcavities by Apodized Stepwise Pulse Anodization

Cheryl Suwen Law, Siew Yee Lim, Raeanne Macalincag, Andrew D. Abell, and Abel Santos

ACS Appl. Nano Mater., **Just Accepted Manuscript** • DOI: 10.1021/acsanm.8b00494 • Publication Date (Web): 28 Aug 2018

ACS Publications

is published by the American Chemical Society. 1155 Sixteenth Street N.W., Washington, DC 20036

Light-Confining Nanoporous Anodic Alumina Microcavities by Apodized Stepwise Pulse Anodization

Cheryl Suwen Law[1,2,3], *Siew Yee Lim*[1,2,3], *Raeanne M. Macalincag*[1], *Andrew D. Abell*[2,3,4*], *and Abel Santos*[1,2,3*]

[1]School of Chemical Engineering, The University of Adelaide, SA 5005 Adelaide, Australia.
[2]Institute for Photonics and Advanced Sensing (IPAS), The University of Adelaide, SA 5005 Adelaide, Australia.
[3]ARC Centre of Excellence for Nanoscale BioPhotonics (CNBP), The University of Adelaide, SA 5005 Adelaide, Australia.
[4]Department of Chemistry, The University of Adelaide, SA 5005 Adelaide, Australia.

*E-mails: andrew.abell@adelaide.edu.au ; abel.santos@adelaide.edu.au

KEYWORDS: Nanoporous Anodic Alumina, Optical Microcavity, Light Confinement, Apodized Anodization, Quality Factor.

ABSTRACT: This study presents an innovative approach to fabricate nanoporous anodic alumina optical microcavities (NAA-μCVs) with enhanced quality factor and versatile optical properties. An apodization strategy using a logarithmic negative function is applied to a stepwise pulse anodization process in order to engineer the effective medium of NAA so it confines light efficiently. The architecture of these light-trapping photonic crystals is composed of two highly reflecting mirrors with asymmetrically apodized effective medium. Various anodization parameters such as anodization time, anodization period, current density offset, and pore widening time are systematically modified to assess their effect on the optical properties of NAA-μCVs in terms of quality factor and position of resonance band. We demonstrate that this fabrication approach enables the generation of NAA-μCVs with high quality factor (~113) and well-resolved and tunable resonance bands across the spectral regions, from UV to NIR, through the manipulation of the anodization parameters. These results represent a comprehensive rationale for the development of high quality NAA-μCVs with enhanced light-confining capabilities, providing new opportunities for further fundamental and applied research across a broad range of fields and disciplines such as photonics and optical sensing.

INTRODUCTION

New materials and structures that effectively confine light to small volumes are central for the development and advancement of nanophotonic applications such as quantum communication and computing[1], nanolasers[2], ultra-small photonic filters[3], and optical sensing.[4] Photons possess no charge or rest mass and are prone to escaping when trapped in photonic structures.[5,6] The confinement of light within small volumes comparable to the wavelength of light is challenging. However, high quality optical microcavities with strong light confinement capabilities to attain the precise control of light emission and propagation have been realized.[7,8] Photonic crystals (PCs) have emerged as the most promising platforms to develop efficient optical microcavities with high quality factor and small cavity volume.[9,10] Optical microcavities (μCVs) are photonic crystal structures that can guide and build up optical signals by light confinement.[6] Typically, μCVs consists of two plane-parallel mirrors positioned apart at a fixed distance with the objective of capturing and storing light indefinitely, until the system is triggered to release the confined light from the cavity in a controlled fashion.[6,11,12] μCVs can be produced in different materials, including polymers[13], semiconductors such as GaAs, InP, GaInAsP and GaN[14-17] and silicon[4,18,19]. Usually, μCVs are fabricated by a combination of lithographic and etching techniques, and chemical or physical vapor deposition.[17] However, alternative materials such as porous silicon produced by electrochemical etching of silicon opened new opportunities to develop nanoporous μCVs with tunable optical properties and nanoporous architectures for different applications, including light-emitting devices, solar cells, optical filters, biosensors, drug delivery and theranostics.[20-22] The modulation of porosity in depth by the anodizing current allows the effective engineering the optical properties of porous silicon μCVs, the composite air-silicon matrix of which acts as a versatile effective medium.[23-27] Porous silicon has outstanding optoelectronic properties, however it has poor chemical stability and mechanical strength and

its fabrication process requires the use of extremely hazardous HF-based electrolytes.[28,29] To date, different alternative/complementary nanoporous materials have been explored to overcome the intrinsic limitations of porous silicon. Of these, nanoporous anodic alumina (NAA) produced by anodization of aluminum has superior properties to those of porous silicon in respect of mechanical, thermal and chemical stabilities as well as versatile nanopore geometry. Furthermore, anodization of aluminum is a well-established electrochemical process performed in mild acid electrolyte solutions that is economical and fully scalable process and requires minimum safety measures.[30-36]

Recent studies have demonstrated that the effective refractive index of NAA can be precisely modulated in a multi-dimensional fashion to create a broad range of PC structures with finely tuned optical properties (e.g. distributed Bragg reflectors, gradient-index filters, bandpass and linear variable bandpass filters, encoded photonic tags, etc.). The realization of NAA-based μCVs has been demonstrated in a few pioneering studies.[37-40] The fabrication of NAA-μCVs involves the introduction of defect modes in the PC structure, which can be achieved by various approaches such as the insertion of a thin layer of nanopores with constant effective refractive index between two highly reflective Bragg mirrors, a phase shift of effective refractive index between Bragg mirrors, or a progressive asymmetric modulation of the effective medium in depth.[37,38,41] However, the maximum quality factors of NAA-μCVs reported by Wang *et al*. (~24)[38], Lee *et al.* (~55)[37] and Yan *et al*. (~45)[41] were found to be significantly lower than those of porous silicon-based μCVs (~1500-3400)[19,42,43] due to the low refractive index of alumina (Al_2O_3 – $n_{Alumina}$~1.70).[37-40] Despite this limitation, the development of new pulse-like anodization strategies and novel NAA-PC architectures provides new opportunities to improve the quality of NAA-μCVs and explore new strategies to attain strong light confinements by a precise control of light–matter interactions at the nanoscale.[37-59] Recently, we identified sharp resonance bands within the photonic stopband

(PSB) of NAA-PCs produced by stepwise pulse anodization when a logarithmic negative apodization function was applied under certain conditions.[60] Motivated by these results, we decided to explore this nanofabrication approach to develop high-quality NAA-μCVs.

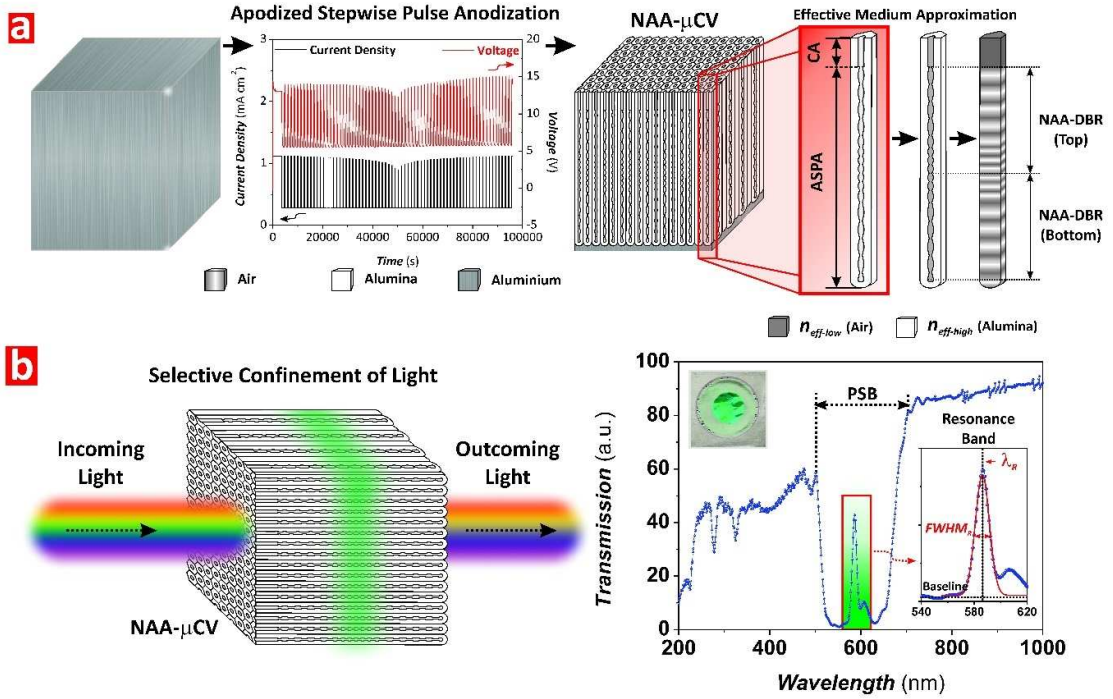

Figure 1. Fabrication of NAA-μCVs by apodized stepwise pulse anodization (ASPA). a) Representative ASPA profile (left) and structure of NAA-μCVs (right) showing details of the existing relationship between nanopore geometry and effective refractive index (n_{eff}) distribution between high (alumina) and low (air) values along the nanopore depth. b) Schematic showing the confinement of light within the structure of NAA-μCVs (left) and representative transmission spectra showing the characteristic photonic stopband (PSB) and the resonance band at its center in NAA-μCVs. Insets show a digital picture of that NAA-μCVs with the characteristic green interferometric color denoting the position of the photonic stopband and a magnified view of the red rectangle showing details of the resonance band (note: NAA-μCV produced with T_P = 1300 s, ΔA_J = 0.210 mA cm^{-2}, J_{Offset} = 0.280 mA cm^{-2}, t_{An} = 25 h, and t_{pw} = 6 min).

In this study, a new architecture of NAA-μCVs that enables high quality confinement of light by means of a rationally designed apodized stepwise pulse anodization (ASPA) approach is presented. A negative apodization function is implemented into the stepwise pulse anodization profile with the aim of modulating the effective refractive index of NAA in depth and engineering the photonic stopband (PSB) of the Bragg mirrors (**Figure 1**).[61,62] Various anodization parameters including anodization time, anodization period, current density offset, and pore widening time are systematically modified in order to maximize and

tune the resonance band of NAA-μCVs across the spectral regions. Our study establishes a comprehensive rationale towards the fabrication of NAA-μCVs with high quality factor and optimized optical properties. These PCs will enable new opportunities to expand the applicability of NAA-μCVs across disciplines such as ultra-sensitive sensors, light harvesting/emitting devices, and optical filters.

EXPERIMENTAL SECTION

2.1. Materials. High purity (99.9997%) aluminum (Al) foils of thickness 0.32 mm were supplied by Goodfellow Cambridge Ltd. (UK). Sulfuric acid (H_2SO_4), perchloric acid ($HClO_4$), copper (II) chloride ($CuCl_2$), hydrochloric acid (HCl), phosphoric acid (H_3PO_4), and ethanol (EtOH-C_2H_5OH) were supplied by Sigma-Aldrich (Australia) and used as received, without further purification steps. Aqueous solutions used in this study were prepared with Milli-Q® water (18.2 mΩ·cm).

2.2. Fabrication of Nanoporous Anodic Alumina Microcavities. NAA optical microcavities (NAA-μCVs) were produced by apodized stepwise pulse anodization (ASPA) under current density control conditions. 1.5 x 1.5 cm Al square chips were cleaned under sonification in EtOH and Milli-Q® water for 15 min each, then dried under air stream. Prior to anodization, these Al substrates were electropolished in a mixture of EtOH and $HClO_4$ 4:1 *(v:v)* at 20 V and 5°C for 3 min. The anodization process of Al substrates was carried out in an electrochemical reactor at a constant temperature of -1°C, using an aqueous solution of 1.1 M H_2SO_4 with 25 *v*% of EtOH as electrolyte. The galvanostatic anodization process started with a constant current density step at 1.120 mA cm^{-2} for 1 h to create a starting nanoporous oxide layer that acts a shuttle for achieving a homogenous pore growth rate preceding the ASPA step. The anodization profile was subsequently set to apodized stepwise pulse mode. A logarithmic negative apodization function was implemented into conventional stepwise pulse

anodization. The current density-time ASPA profiles were produced by a custom-designed Labview®-based software according to **Equation 1**.

$$J(t) = 2A_J(t) + J_{offset} \quad (1)$$

where $A_J(t)$ is the time-dependent current density amplitude, which follows a logarithmic negative apodization function as defined in **Equations 2 and 3**.

For $t \leq t_{An}/2$

$$A(t)_J = A_{max} + \left(\frac{A_{min} - A_{max}}{\log\left(\frac{t_{An}}{2}+10\right)-1}\right).(\log(t+10)-1) \quad (2)$$

For $t > t_{An}/2$

$$A(t)_J = \left(\frac{A_{max} - A_{min}}{\log(t_{An}+10)-\log\left(\frac{t_{An}}{2}+10\right)}\right).\left(\log(t+10)-\log\left(\frac{t_{An}}{2}+10\right)\right) + A_{min} \quad (3)$$

where A_{max} and A_{min} are the maximum and minimum amplitudes and t_{An} is the total anodization time at ASPA.

Note that T_P in the ASPA profile was defined as the total time length of high and low anodization current density pulses (**Equation 4**):

$$T_p = t_{high} + t_{low} \quad (4)$$

where t_{high} and t_{low} are the time duration at high and low current density values, respectively. The ratio between t_{high} and t_{low} was set to t_{high}:t_{low} = 1:4.

To gain a better understanding of the light-confining capabilities of NAA-μCVs produced by ASPA, different anodization parameters (i.e. anodization time –t_{An}, anodization period –T_P, current density offset –J_{offset}, and pore widening time –t_{pw}) were systematically manipulated

to assess their effects on the optical characteristics of NAA-μCVs, such as interferometric color, position of the resonance band (λ_R), full-width at half maximum of the resonance band ($FWHM_R$) and quality factor of cavity (Q_C), as defined by **Equation 5**.

$$Q_C = \frac{\lambda_R}{FWHM_R} \tag{5}$$

2.3. Optical Characterization. Prior to optical characterization, the remaining aluminum substrate was selectively dissolved from the backside of these aluminum chips by wet chemical etching in a saturated solution of $HCl/CuCl_2$, using an etching cell with a Viton® mask with a circular window of 5 mm in diameter. These etched NAA-μCVs were then optically characterized. The optical transmission spectra of NAA-μCVs fabricated at various conditions were obtained at normal incidence (i.e. θ = 0°) from 200–1000 nm with a resolution of 1 nm and 5 mm slit using a UV-vis-NIR spectrophotometer (Cary 60, Agilent, USA), and from 200–1500 nm with a resolution of 1 nm in a UV-vis-NIR spectrometer (UV-3600 Plus, Shimadzu, Japan). The interferometric color displayed by these NAA-μCVs as a function of the different fabrication parameters was characterized through digital images acquired by a Canon EOS 700D digital camera equipped with a Tamron 90 mm F2.8 VC USD macro mount lens with autofocus function under natural illumination. A black card was used as background for the digital image acquisition. The pore size of NAA-μCVs was widened by isotropic chemical etching in an aqueous solution of 5 *wt%* H_3PO_4 at 35°C at different pore widening times (i.e. t_{pw} = 0, 2, 4, and 6 min) and their transmission spectra and digital images were recorded after each pore widening step. Note that the features of the resonance band of these NAA-μCVs (i.e. position of resonance band –λ_R, full-width at half maximum of the resonance band –$FWHM_R$, and baseline of resonance band – y_0) were estimated using OriginPro 8.5®, applying Gaussian fittings over the resonance bands shown in the transmission spectra of NAA-μCVs and using as a baseline the lower lobe of the

photonic stopband (PSB), as illustrated in **Figure 1**. The obtained results were summarized in contour maps generated using OriginPro 8.5®, using a triangulation algorithm in which the coordinates of the intersection point were computed with linear interpolation.

2.4. Structural Characterization. The nanoporous structure of NAA-μCVs was characterized by a field emission gun scanning electron microscope (FEG-SEM FEI Quanta 450). The obtained FEG-SEM images were analyzed using ImageJ (public domain program developed at the RSB of the NIH).[63]

RESULTS AND DISCUSSION

3.1. Fabrication and Structural Characterization of Nanoporous Anodic Alumina Microcavities. Figure 1a illustrates the fabrication process of NAA-μCVs by ASPA. The structure of these PC structures is composed of two highly reflective distributed Bragg reflector (DBR) mirrors with asymmetrically modulated effective refractive index in a stepwise fashion in depth following a logarithmic negative window. The amplitude of the current density pulse is logarithmically reduced during the fabrication process of the first half of the NAA-μCV (i.e. from $t = 0$ to $t = t_{An}/2$) (**Equation 2**). At $t = t_{An}/2$, the current density amplitude is progressively increased according to the mathematical expression shown in **Equation 3**. The transmission spectrum of these PC structures is characterized by a relatively broad PSB with a strong and narrow resonance band at approximately its central position (**Figure 1b**). This resonance band denotes a strong confinement of light within the NAA-μCV at that narrow range of wavelengths, which is established by the geometric features of the NAA-DBR mirrors. **Figures 2a-c** show a set of representative FEG-SEM images of NAA-μCVs produced by ASPA. These images reveal that the structure of these PCs is composed of stacked layers of NAA with a porosity modulation in depth that follows the ASPA current density profile applied during the anodization process. **Figure 2a** depicts a

representative top view FEG-SEM image of a NAA-μCV, revealing nanopores with an average pore diameter (d_p) of 15 ± 2 nm that are randomly distributed across the surface.

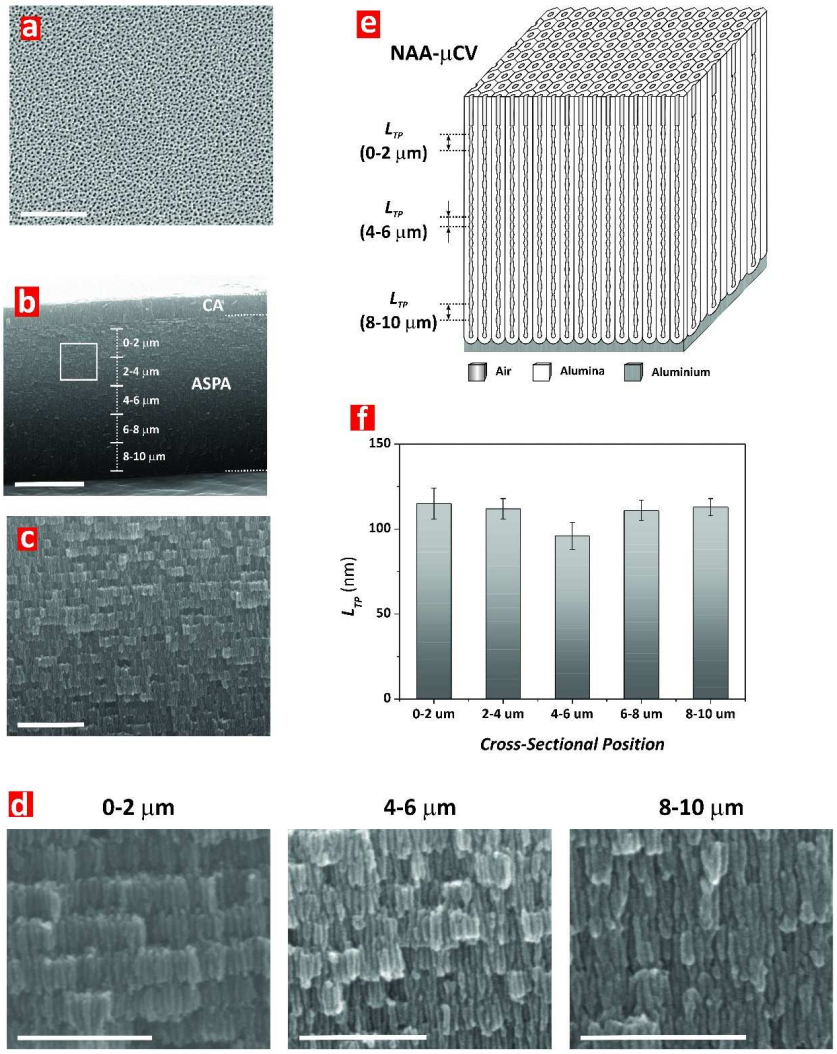

Figure 2. Nanoporous structure of NAA-μCVs produced by ASPA. a) Representative top view FEG-SEM image of a NAA-μCV showing a random distribution of nanopores with d_P = 15 ± 2 nm (scale bar = 500 nm). b) General cross-sectional view FEG-SEM image of a NAA-μCV showing a top layer of straight nanopore diameter (constant anodization = CA – thickness = 1.4 ± 0.1 μm) and the PC microcavity layer with nanopore dimeter modulation (ASPA – thickness = 11.0 ± 0.1 μm) with details showing the areas where the period length (L_{TP}) was estimated (i.e. from 0-2 μm to 8-10 μm) (scale bar = 5 μm). c) Magnified view of the white rectangle shown in (b) revealing the porosity modulation in depth in NAA-μCVs (scale bar = 1 μm). d) Magnified views at different cross-sectional positions (i.e. 0-2, 4-6, and 8-10 μm) showing details of the period length modulation (scale bar = 500 nm). e) Illustration representing the idealized nanoporous structure of NAA-μCVs, where the period length (L_{TP}) is modified in depth to create an optical microcavity structure with a logarithmically modulated effective refractive index composed of two NAA-DBRs with asymmetrically modulated effective refractive index. f) Bar chart showing the period length distribution in NAA-μCVs produced by ASPA along the nanopore depth (note: NAA-μCV produced with T_P = 800 s, ΔA_J = 0.210 mA cm^{-2}, J_{Offset} = 0.280 mA cm^{-2}, t_{An} = 20 h, and t_{pw} = 6 min).

Figure 2b shows a general cross-sectional view of a NAA-μCV produced with T_P = 800 s, J_{offset} = 0.280 mA cm^{-2}, ΔA_J = 0.210 mA cm^{-2}, t_{An} = 10 h, and t_{pw} = 6 min. That image reveals that the structure of these NAA-μCVs is composed of a top layer 1.4 ± 0.1 μm thick with constant nanopore diameter, which results from the first anodization stage at constant anodizing current density (CA – J = 1.120 mA cm^{-2} for 1 h), and a much thicker layer (i.e. 11.0 ± 0.1 μm) with nanopore diameter modulation in depth corresponding to the ASPA stage (**Figures 2c and d**). A pore branching effect can be observed at the bottom part of the NAA-μCV structure (**Figure 2d**; 8-10 μm), which can be associated with the non-self-organization conditions used in our study. A closer analysis of the period length (i.e. L_{TP} – distance between adjacent layers in the ASPA section of the NAA-μCVs) reveals a direct dependency with the anodization amplitude (ΔA_J) (**Figure 2e**). For instance, we estimated the average L_{TP} along the ASPA cross-section of a NAA-μCV produced with T_P = 800 s, J_{offset} = 0.280 mA cm^{-2}, ΔA_J = 0.210 mA cm^{-2}, t_{An} = 10 h, and t_{pw} = 6 min every 2 μm by FEG-SEM image analysis. Our results indicate that L_{TP} varies along the nanopore depth following the apodization function applied during anodization, with an estimation of 115 ± 9 nm at 0–2 μm, 112 ± 6 nm at 2–4 μm, 96 ± 8 nm at 4–6 μm, 111 ± 6 nm at 6–8 μm, and 113 ± 5 nm at 8–10 μm (**Figure 2f**). From this analysis it is apparent that L_{TP} is reduced at the center of the ASPA section of the NAA-μCVs (i.e. $t \sim t_{An}/2$), which is expected due to the significant reduction of the anodization amplitude at $t = t_{An}/2$. Furthermore, FEG-SEM image analysis denote a modulation of porosity in depth with the pulse anodizing current density. For instance, the porosity at J = 0.280 and 1.120 mA cm^{-2} (i.e. minimum and maximum values of current density) was estimated to be 18 ± 9 and 32 ± 13%, respectively.[48] Apodization is a filtering technique broadly used in optics to narrow the PSB of photonic structures. The direct relationship between the geometric features of NAA-μCVs and the anodization parameters

enables the apodization of the optical signals of these PCs by structural engineering of their effective medium (i.e. effective refractive index modulation).

3.2. Effect of Anodization Time (t_{An}) on the Optical Properties of Nanoporous Anodic Alumina Microcavities. To understand the effect of t_{An} on the optical characteristics of NAA-μCVs, a set of NAA-μCVs was fabricated using logarithmic negative ASPA with varying t_{An} from 5 to 25 h at an interval of 5 h. Other anodization parameters such as anodization period (T_P), current density offset (J_{offset}), and amplitude difference (ΔA_J) were fixed at 1200 and 1300 s, 0.280 mA cm^{-2}, and 0.210 mA cm^{-2}, respectively. **Figures 3a and b** show representative anodization profiles for NAA-μCVs fabricated at different t_{An} (i.e. 5, 10, 15, 20, and 25 h) for T_P = 1200 and 1300 s, respectively. These ASPA profiles denote that, under the anodization conditions used in our study, the anodizing current density profile is precisely translated into modulations of voltage throughout the whole process, resulting in an internal modulation of d_p in depth. The transmission spectra of NAA-μCVs produced at T_P = 1300 s as a function of t_{An} and pore widening time (t_{pw}) are displayed in **Figures 4a-e**. The optical properties of these NAA-μCVs were characterized in terms of λ_R, $FWHM_R$, Q_c, and interferometric color. **Figure 4** shows that the PSB of these NAA-μCVs is located within visible-NIR range and it undergoes a blue shift and increases its intensity and width with t_{pw}, from 0 to 6 min. The interferometric color is a result of the selective and constructive reflection of light by the NAA-μCV structure and denotes the position of the PSB within the UV (transparent), visible (color), or NIR (transparent) spectral regions. The transmission spectra of these NAA-μCVs shows a resonance band located at approximately the center of the PSB, which indicates the presence of an optical microcavity within the structure of these PCs.

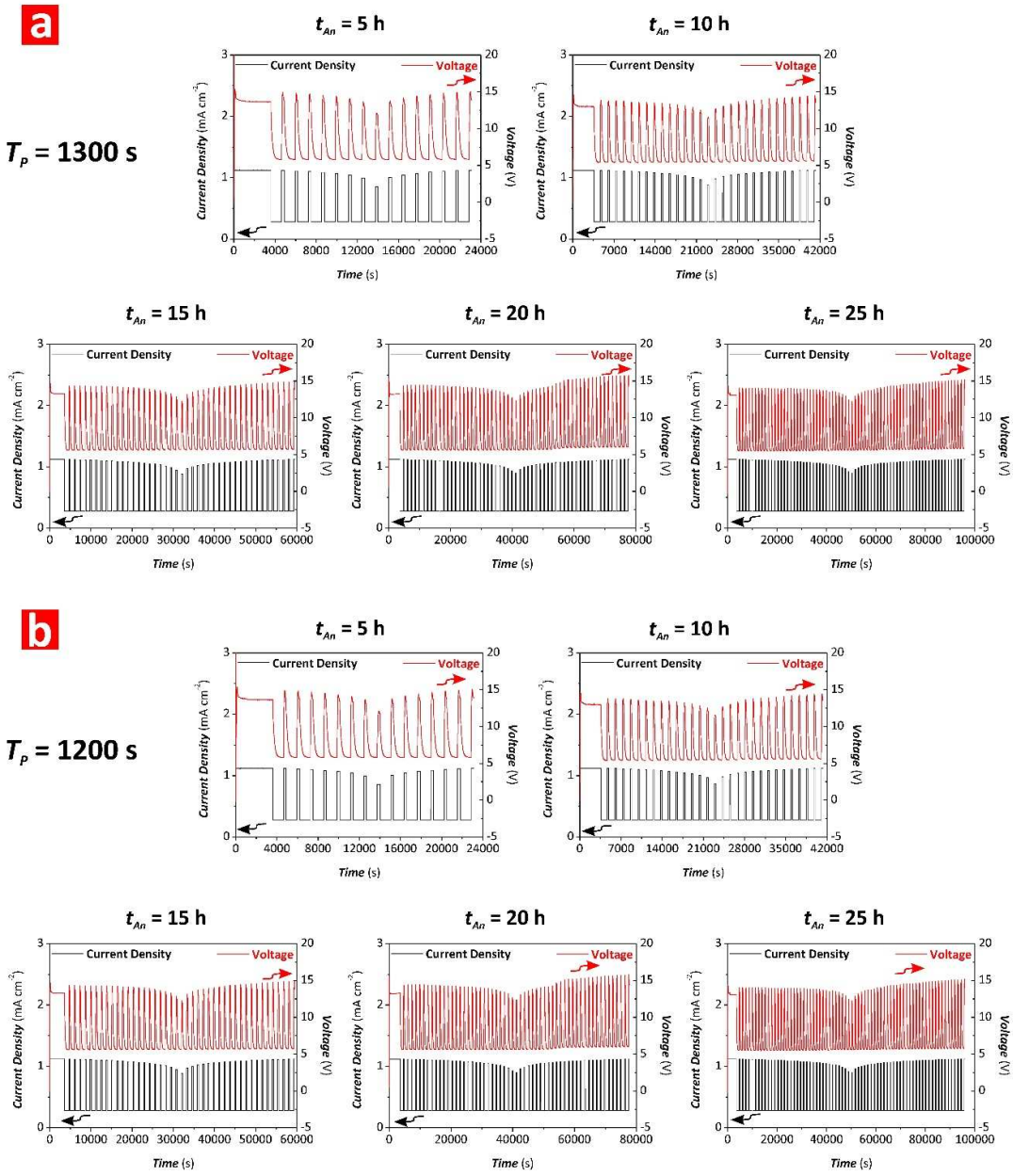

Figure 3. Representative anodization profiles of NAA-μCVs produced by ASPA at different anodization times and anodization periods (note: NAA-μCVs produced with T_P = 1200 and 1300 s, ΔA_J = 0.210 mA cm^{-2} and J_{Offset} = 0.280 mA cm^{-2}). a) Anodization profiles of NAA-μCVs produced with T_P = 1300 at t_{An} = 5, 10, 15, 20, and 25 h. b) Anodization profiles of NAA-μCVs produced with T_P = 1200 at t_{An} = 5, 10, 15, 20, and 25 h.

Figures 5a-e show magnified views of the resonance bands observed in the transmission spectra of these NAA-μCVs (**Figures 4a-e**) with details of Gaussian fittings used to estimate λ_R, $FWHM_R$, and Q_c. In general, it can be observed that the resonance band of these NAA-

μCVs rises as t_{pw} increases, becoming more well-resolved and intense due to the effective refractive index contrast enhancement between adjacent NAA layers.

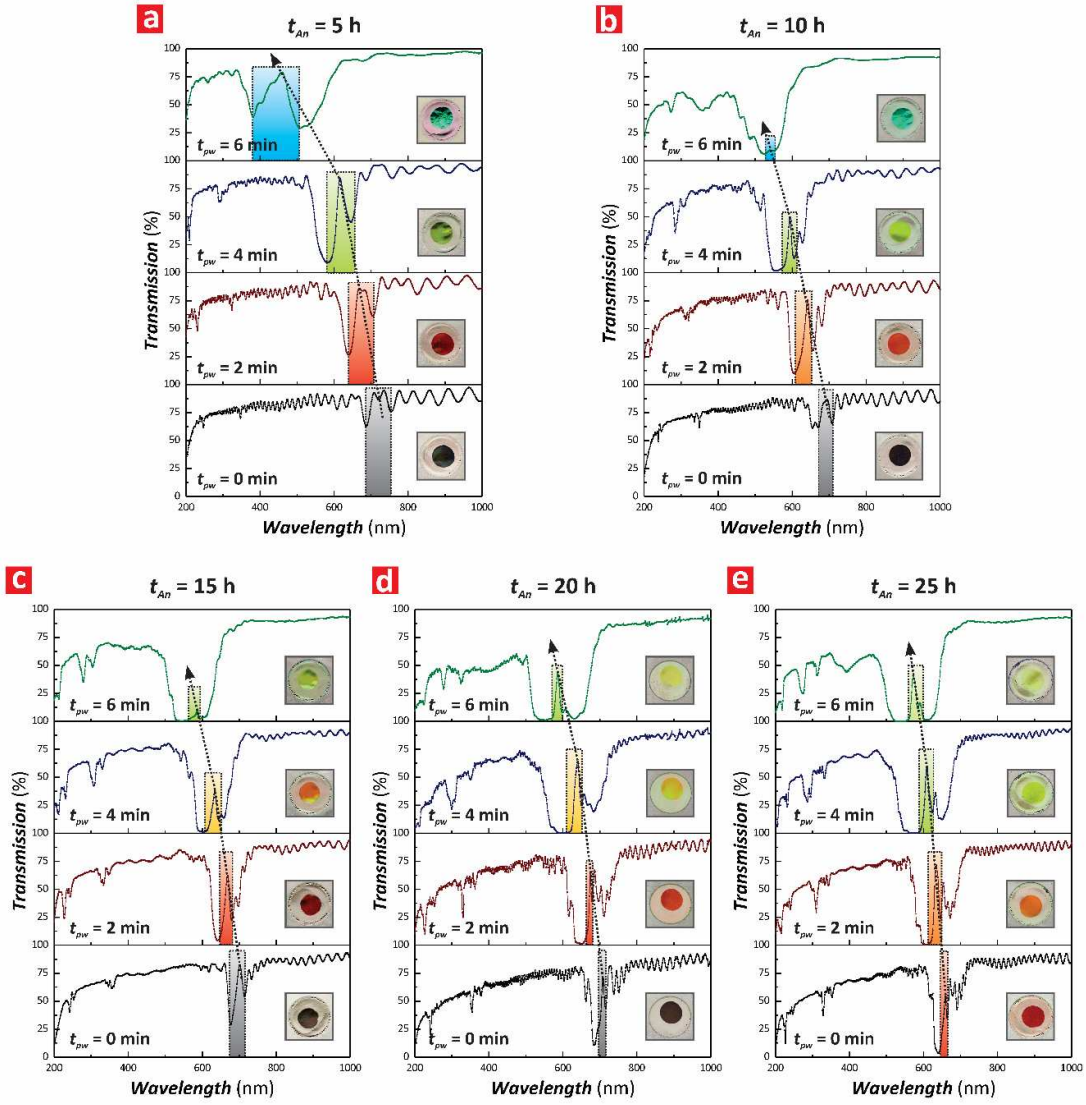

Figure 4. Combinational effect of anodization time (t_{An}) and pore widening time (t_{pw}) on the transmission spectrum of NAA-μCVs produced by ASPA at T_P = 1300 s (note: color rectangles denote the approximate position of the resonance band within the PSB and black dotted arrow lines indicate the blue shift of the resonance bands with t_{pw}). a) t_{An} = 5, b) t_{An} = 10, c) t_{An} = 15, d) t_{An} = 20, and e) t_{An} = 25 h. Insets in a-e display digital pictures of these photonic crystal structures showing vivid interferometric colors when the resonance band is located within the visible region and transparent when the band is within the UV or NIR spectral regions.

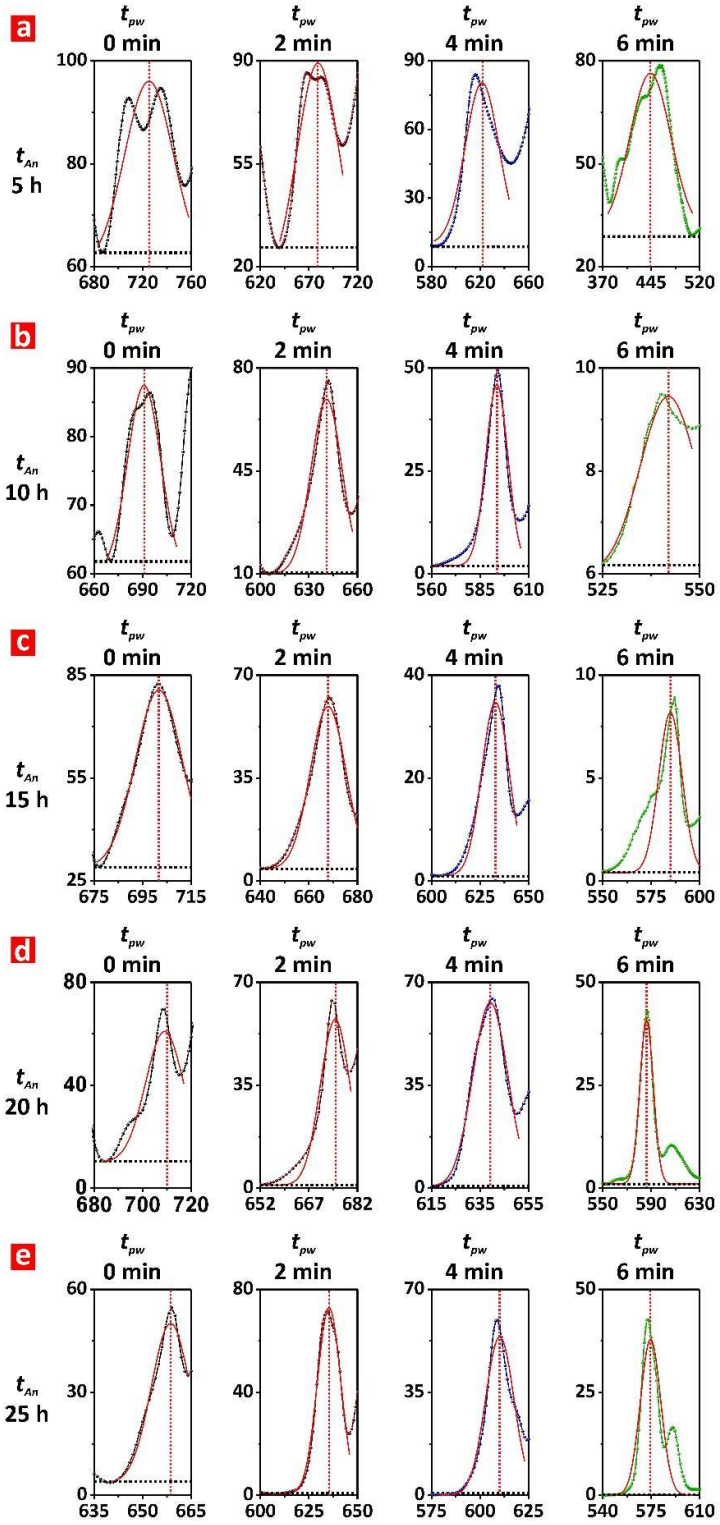

Figure 5. Combinational effect of anodization time (t_{An}) and pore widening time (t_{pw}) on the resonance band of NAA-μCVs produced by ASPA at T_P = 1300 s (note: horizontal dotted black lines denote the baseline (y_0) used for the Gaussian fittings, which correspond to the lower lobe of the PSB, and vertical dotted red lines indicate the central wavelength of the resonance band (λ_R) and the symmetry of the Gaussian fitting). a) t_{An} = 5, b) t_{An} = 10, c) t_{An} = 15, d) t_{An} = 20, and e) t_{An} = 25 h.

The stepwise modulation of nanopores within NAA-μCVs is more evident as the nanoporous structure of NAA is chemically etched, since those layers produced at lower anodizing current density dissolve at a faster rate than those produced at higher J (**Figure S1 – Supporting Information**). However, the over-etching of the NAA-μCVs' structure ($t_{pw} > 4$ min) results in a broadening of the resonance band and a decrement of its intensity due to light scattering by the overall PC structure (**Figure S2 – Supporting Information**). So, for NAA-μCVs produced at t_{An} = 5, 10, and 15 h, the resonance band is almost vanished from the transmission spectrum at t_{pw} = 6 min. To further extend the analysis on the effect of t_{An} on the optical properties of NAA-μCVs produced by ASPA, we fabricated another set of NAA-μCVs under the same conditions (i.e. J_{offset} = 0.280 mA cm^{-2}, ΔA_J = 0.210 mA cm^{-2}, and t_{An} = 5, 10, 15, 20, and 25 h) but setting the anodization period at T_P = 1200 s. **Figure 3b** shows representative anodization profiles of these NAA-μCVs produced at T_P = 1200 s, showing how the anodizing current density (input) is directly translated into voltage (output) changes in a dynamic fashion, without apparent delay. **Figures 6a-e** show the transmission spectra of NAA-μCVs produced with T_P = 1200 s, which also include digital pictures displaying the characteristic interferometric color of these PC structures. As these graphs indicate, the PSB of these NAA-μCVs is located within the visible-NIR region of the spectrum, although slightly blue-shifted as compared to their T_P = 1300 s counterparts. As demonstrated in previous studies, this blue shift is associated with the reduction of the anodization period, which results in a shorter period length (L_{TP}) within the nanoporous structure of NAA-μCVs.[43-59] The transmission spectra of these NAA-μCVs displays a PSB that increases its intensity with t_{pw} and a well-defined resonance band at the center of the PSB. **Figures 7a-e** compile magnified views of the resonance bands observed in the transmission spectra of these NAA-μCVs (**Figures 6a-e**), with details of Gaussian fittings used to estimate λ_R, $FWHM_R$, and Q_c.

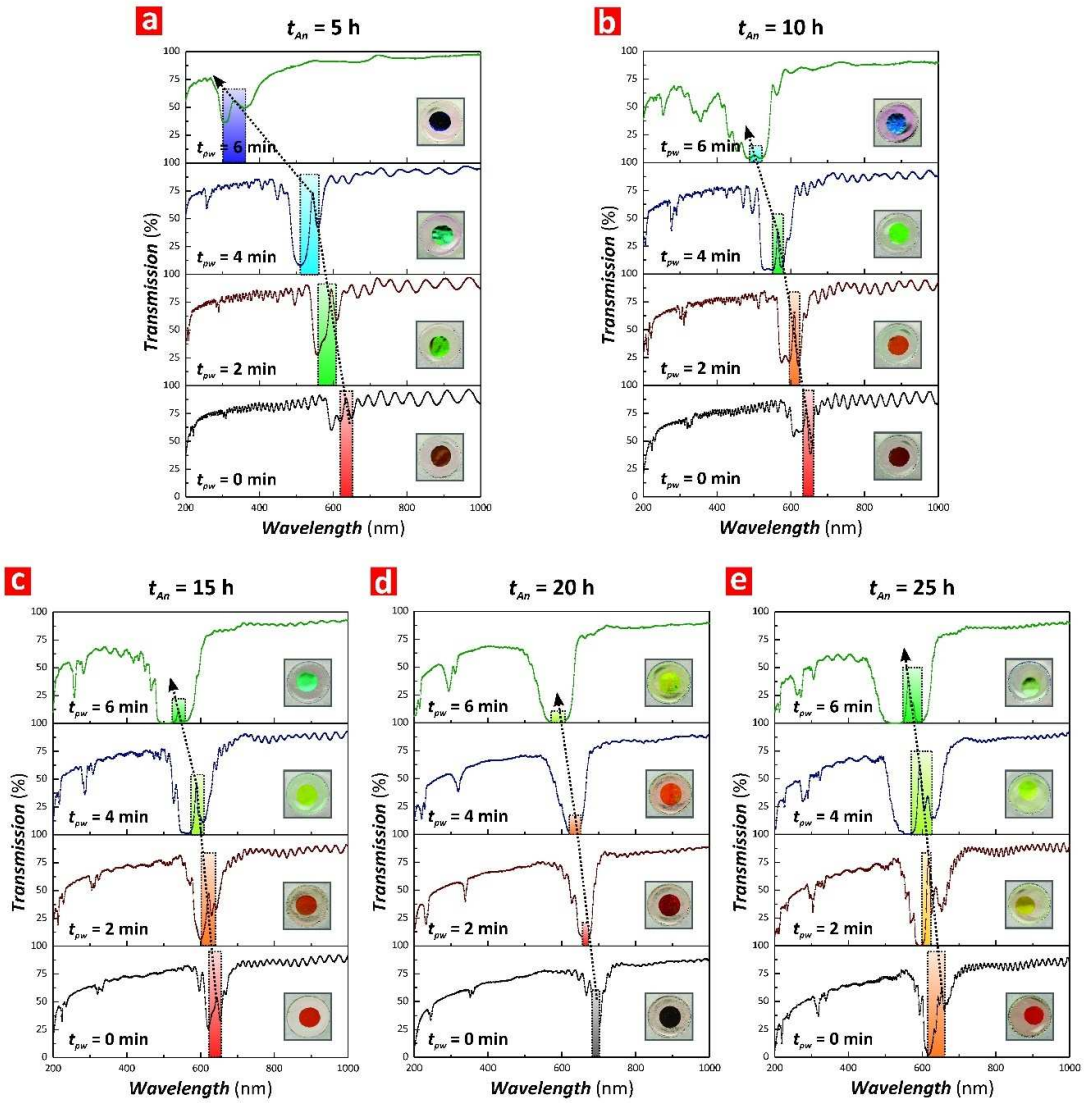

Figure 6. Combinational effect of anodization time (t_{An}) and pore widening time (t_{pw}) on the transmission spectrum of NAA-μCVs produced by ASPA at T_P = 1200 s (note: color rectangles denote the approximate position of the resonance band within the PSB and black dotted arrow lines indicate the blue shift of the resonance bands with t_{pw}). a) t_{An} = 5, b) t_{An} = 10, c) t_{An} = 15, d) t_{An} = 20, and e) t_{An} = 25 h. Insets in a-e display digital pictures of these photonic crystal structures showing vivid interferometric colors when the resonance band is located within the visible region and transparent when the band is within the UV or NIR spectral regions.

The quality factor (Q_C), defined as the ratio of the resonance band wavelength (λ_R) to its full width at half maximum ($FWHM_R$) (**Equation 5**), is an important criteria in assessing the strength of photon confinement within optical microcavities.[64,65] The Q_C of these NAA-μCVs was estimated by fitting the resonance bands shown in **Figures 5 and 7** to Gaussian envelopes, using as a baseline the lower love of the PSB as indicated by the horizontal dotted black lines showed in these graphs.

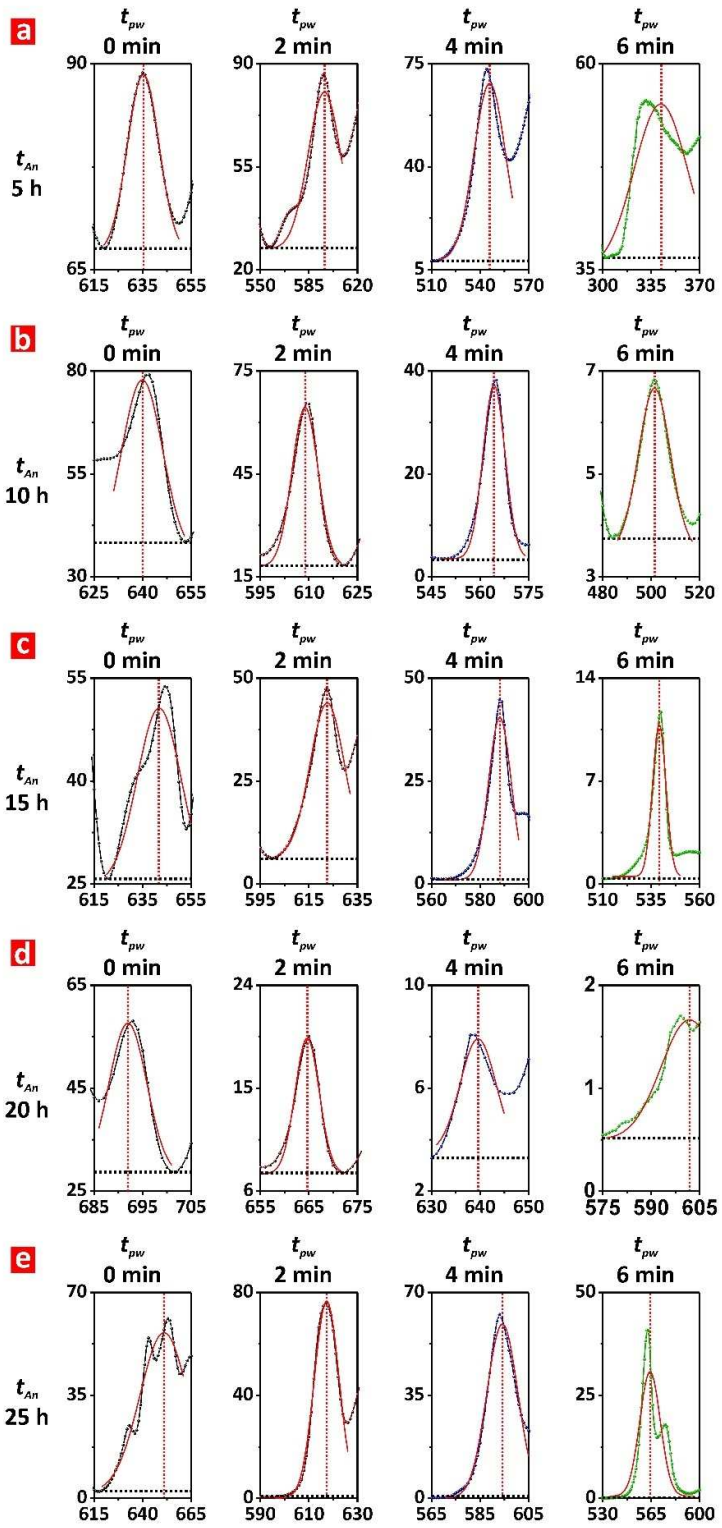

Figure 7. Combinational effect of anodization time (t_{An}) and pore widening time (t_{pw}) on the resonance band of NAA-μCVs produced by ASPA at T_P = 1200 s (note: horizontal dotted black lines denote the baseline (y_0) used for the Gaussian fittings, which correspond to the lower lobe of the PSB, and vertical dotted red lines indicate the central wavelength of the resonance band (λ_R) and the symmetry of the Gaussian fitting). a) t_{An} = 5, b) t_{An} = 10, c) t_{An} = 15, d) t_{An} = 20, and e) t_{An} = 25 h.

A summary of the estimated values of y_0, λ_R, $FWHM_R$ and Q_C are compiled in **Tables S1-S3 (Supporting Information)** along with the quality (R^2) of these Gaussian fittings. **Figure 8** shows contour maps summarizing the dependency of Q_C and λ_R with t_{An} and t_{pw} for NAA-μCVs produced with T_P = 1200 and 1300 s, J_{offset} = 0.280 mA cm^{-2}, and ΔA_J = 0.210 mA cm^{-2}. **Figure 8a** shows the dependency of Q_C on t_{An} and t_{pw} for NAA-μCVs fabricated with T_P = 1300 s. It is apparent that Q_C becomes more dependent on these fabrication parameters at short pore widening times (i.e. from t_{pw} = 0 to 2 min) and longer anodization times (i.e. from t_{An} = 15 to 25 h). This trend is denoted by a closer and denser concentration of color fields around the Q_C maximum (i.e. Q_C = 63.1 ± 1.2), which is located at t_{pw} = 2 min and t_{An} = 20 h. In general, an increase in t_{An} leads to an enhancement of the Q_C of NAA-μCVs, while longer pore widening times worsen the quality factor of the NAA-μCVs. The relationship between λ_R with t_{An} and t_{pw} for NAA-μCVs produced with T_P = 1300 s is displayed in **Figure 8b**, where it can be clearly observed that the distance between color fields is closer as t_{An} is reduced from 10 to 5 h. This indicates a strong dependency of λ_R with t_{An} at shorter anodization times. Furthermore, it is observed that λ_R is blue-shifted with t_{pw} across the UV-visible spectrum from t_{An} = 5 to 25 h. This analysis also reveals that the effect of t_{An} on the position of the resonance band is not as significant as that of t_{pw}, since only a slight red shift is observed as t_{An} increases from 5 to 20 h, and a slight blue shift from 20 to 25 h, achieving its maximum value (i.e. 725 ± 1 nm) at t_{An} = 5 h and t_{pw} = 0 min. The distribution of Q_c and λ_R for NAA-μCVs produced at T_P = 1200 s with t_{An} and t_{pw} is presented in **Figures 8c and d**, respectively. The contour map shown in **Figure 8c** reveals a concentration of color fields at the region of longer t_{An} and shorter t_{pw}, achieving a local maximum of Q_C (i.e. 112.6 ± 5.2) at t_{An} = 20 h and t_{pw} = 2 min, which is the highest quality factor reported for a NAA-based optical microcavity to date.

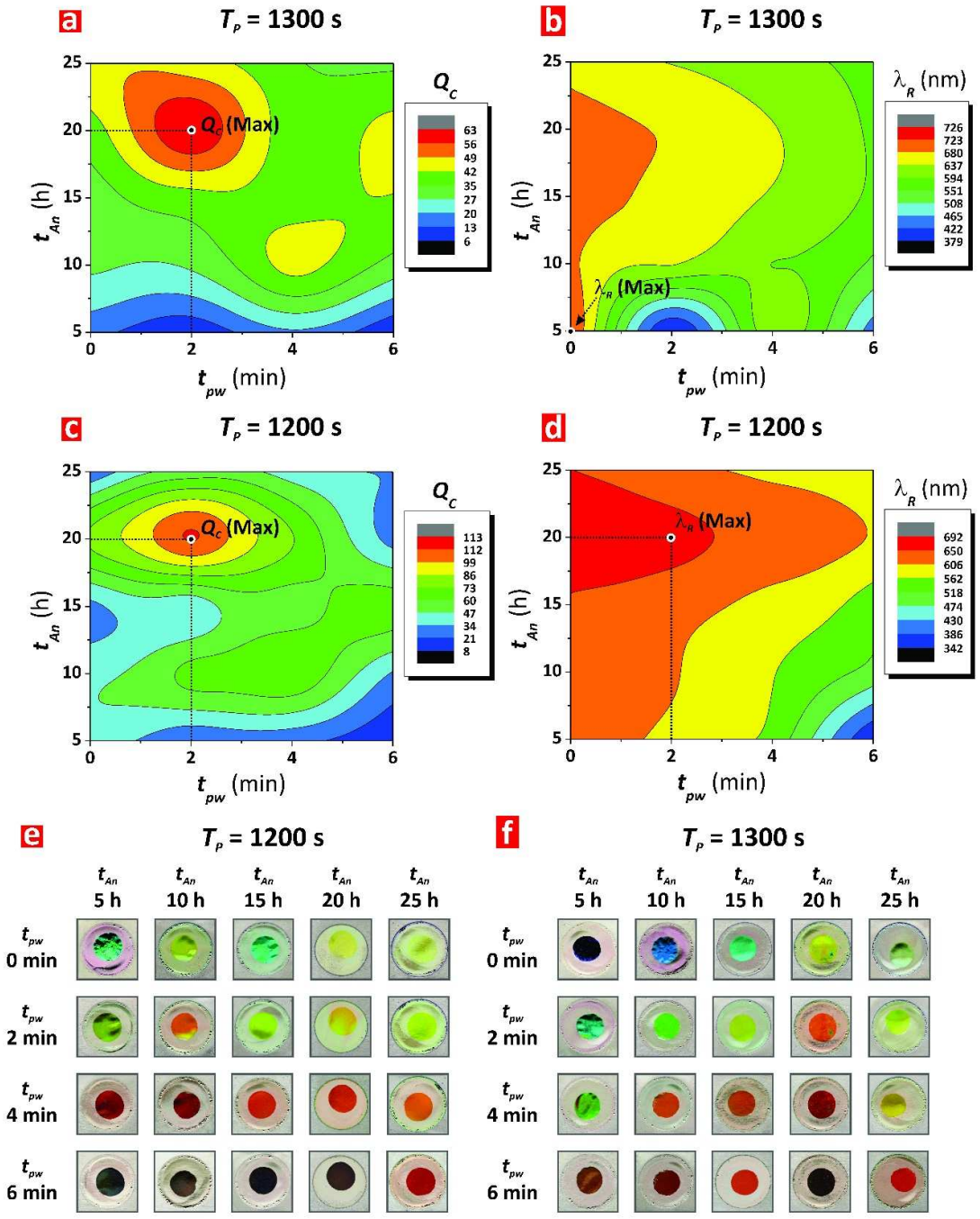

Figure 8. Combinational effect of anodization time (t_{An}) and pore widening time (t_{pw}) on the optical properties of NAA-μCVs (i.e. quality factor – Q_C, position of resonance band – λ_R, and interferometric color) produced by ASPA. a) Contour map showing the dependency of Q_C with t_{An} and t_{pw} for NAA-μCVs produced with T_P = 1300 s. b) Contour map showing the dependency of λ_R with t_{An} and t_{pw} for NAA-μCVs produced with T_P = 1300 s. c) Contour map showing the dependency of Q_C with t_{An} and t_{pw} for NAA-μCVs produced with T_P = 1200 s. d) Contour map showing the dependency of λ_R with t_{An} and t_{pw} for NAA-μCVs produced with T_P = 1200 s. e) Digital images showing the interferometric color displayed by NAA-μCVs produced with T_P = 1200 s as a function of t_{An} and t_{pw}. f) Digital images showing the interferometric color displayed by NAA-μCVs produced with T_P = 1300 s as a function of t_{An} and t_{pw}.

The distance between field lines around the local maximum is shorter, indicating a stronger dependency of Q_C on t_{An} and t_{pw} around that set of fabrication conditions. In contrast, the combination of shorter t_{An} (i.e. 5 to 15 h) and longer t_{pw} (i.e. 4 to 6 min) worsens Q_C as the distance between field lines and color fields is relatively broad at these areas. **Figure 8d** shows how t_{An} and t_{pw} affect λ_R of NAA-μCVs produced at T_P = 1200 s. This graph denotes a homogenous but broad distribution of color fields with equidistant field lines throughout, from t_{An} = 5 to 25 h and from t_{pw} = 0 to 4 min, which indicates a weak dependency of λ_R on t_{An} and t_{pw} at these combinations of fabrication parameters. As t_{pw} increases from 4 to 6 min and t_{An} decreases from 10 to 5 h, λ_R shows a stronger dependency with these parameters, as suggested by the closer field lines and high density of color fields. λ_R is red-shifted as t_{An} increases from 5 to 20 h and slightly blue-shifted when t_{An} increases from 20 to 25 h. The maximum value of λ_R (i.e. 665 ± 1 nm) is achieved at t_{An} = 20 h and t_{pw} = 2 min. Furthermore, this analysis also reveals that t_{pw} blue-shifts the resonance band of NAA-μCVs produced at T_P = 1200 s as t_{pw} increases. The comparative analysis of **Figures 8a and c** reveals that a combination of long t_{An} (i.e. from 15 to 25 h) and short t_{pw} (i.e. from 0 to 2 min) results in high quality NAA-μCVs with narrow and well-resolved resonance bands. The average Q_C estimated for NAA-μCVs produced with T_P = 1200 and 1300 s were 46.4 ± 24.8 and 33.7 ± 13.8, respectively. It is worthwhile noting that only one of the NAA-μCVs produced at 1300 s showed superior light-confining performance than those reported in previous studies (i.e. Q_C = 63.1 ± 1.2 for NAA-μCV produced with T_P = 1300 s, t_{pw} = 2 min and t_{An} = 20 h – Wang *et al*. (~24)[38], Lee *et al.* (~55)[37] and Yan *et al*. (~45)[41]). However, up to six NAA-μCVs produced with T_P = 1200 s showed superior properties to confine light than previously NAA-based optical microcavities (i.e. Q_C = 64.0 ± 1.0 at t_{pw} = 2 min and t_{An} = 10 h, Q_C = 70.5 ± 2.1 at t_{pw} = 4 min and t_{An} = 10 h, Q_C = 66.0 ± 1.3 at t_{pw} = 6 min and t_{An} = 15 h, Q_C = 75.2 ± 3.1 at t_{pw} = 0 min and t_{An} = 20 h, Q_C = 112,6 ± 5.2 at t_{pw} = 2 min and t_{An} = 20 h, and Q_C = 73.5 ± 2.6

at t_{pw} = 4 min and t_{An} = 20 h). Although both types of NAA-μCVs have a weak correlation between the shift in λ_R with t_{An}, **Figures 8b and d** show that the λ_R of NAA-μCVs produced at T_P = 1300 s evolves in a slightly different manner with t_{An} as compared to NAA-μCVs fabricated at T_P = 1200 s. This graph also indicates that, as observed in the transmission spectra (**Figures 4 and 6**) the position of the PSB and resonance bands of NAA-μCVs produced at T_P = 1200 s is blue-shifted as compared to their equivalent NAA-μCVs fabricated at T_P = 1300 s. It is also observed that both sets of NAA-μCVs show a stronger dependency of λ_R with t_{pw} than that shown for t_{An}. A pore widening treatment blue-shifts the position of the respective resonance bands, and the longer t_{pw} is, the shorter the wavelength where the resonance band is positioned at. It is worthwhile to note that, for a given t_{pw}, the position of the resonance band of NAA-μCVs at T_P = 1300 s is located at longer wavelengths than that of NAA-μCVs produced with T_P = 1200 s due to the red shift associated with the longer anodization period and longer period length. Another interesting optical property of NAA-μCVs is their vivid interferometric colors, which correspond to the wavelength of their respective PSB and λ_R when these are positioned within the visible range of the spectrum. **Figures 8e and f** compile digital images of NAA-μCVs produced at T_P = 1200 and 1300 s as a function of t_{An} and t_{pw}, respectively. The analysis of these images is in good agreement with the results obtained in **Figures 8b and d**, where the λ_R is blue-shifted with t_{pw}. It is also apparent that λ_R is red-shifted with increasing t_{An} from 5 to 20 h and slightly blue shifted from t_{An} = 20 to 25 h.

3.3. Effect of Anodization Period (T_P) on the Optical Properties of Nanoporous Anodic Alumina Microcavities. To demonstrate the tuneability of the position of the resonance band across the spectral regions and to further optimize the quality of NAA-μCVs produced by ASPA, we produced a set of NAA-μCVs with different T_P, where this fabrication parameter

was systematically modified from 800 to 1300 s with ΔT_P = 100 s, while keeping constant J_{offset} and ΔA_J at 0.280 mA cm^{-2} and 0.210 mA cm^{-2}, respectively. The anodization profiles and transmission spectra of these NAA-μCVs are shown in **Figure S3 (Supporting Information)** and **Figure 9**, respectively. **Figures 9a-d** show the transmission spectra of these NAA-μCVs as a function of T_P and t_{pw} (i.e. from 0 to 6 min) and **Figure 10** shows magnified views of the resonance bands and Gaussian fittings used to estimate λ_R, $FWHM_R$ and Q_C. In all these cases it is verified that the PSB and resonance band of theses NAA-μCVs is red-shifted with T_P and blue shifted with t_{pw}. Note that those NAA-μCVs produced with T_P > 800 s also showed second and third order PSBs. NAA-μCVs fabricated with T_P = 900 s have both first and second order PSBs, while NAA-μCVs produced at T_P = 1000, 1100, 1200 and 1300 s show second and third order PSBs. However, the first order PSB plays the primary role in determining the optical properties of NAA-μCVs since this band is much more intense and well-resolved than their higher order counterparts. At t_{pw} = 0 min (**Figure 9a**), all NAA-μCVs display a weak resonance band within their first order PSB, which is in the range of 400 to 700 nm and red-shifted with T_P. As T_P increases, the intensity of the resonance band increases and shifts its position (λ_R) toward the NIR spectral region. As the digital pictures shown in **Figures 9a-d** (insets) indicate, for a given t_{pw} the interferometric color of these NAA-μCVs is red-shifted with T_P. For instance, at t_{pw} = 0 min, the interferometric color of NAA-μCVs changes from transparent (i.e. UV region) (T_P = 800 s), blue (T_P = 900 s), green (T_P = 1000 s), orange (T_P = 1100 s) to transparent (i.e. NIR region) (T_P = 1200 and 1300 s) as T_P increases. It is also verified that the resonance band increases its intensity and it is blue-shifted with a pore widening treatment (i.e. t_{pw} increases), which is in good agreement with our previous observation.

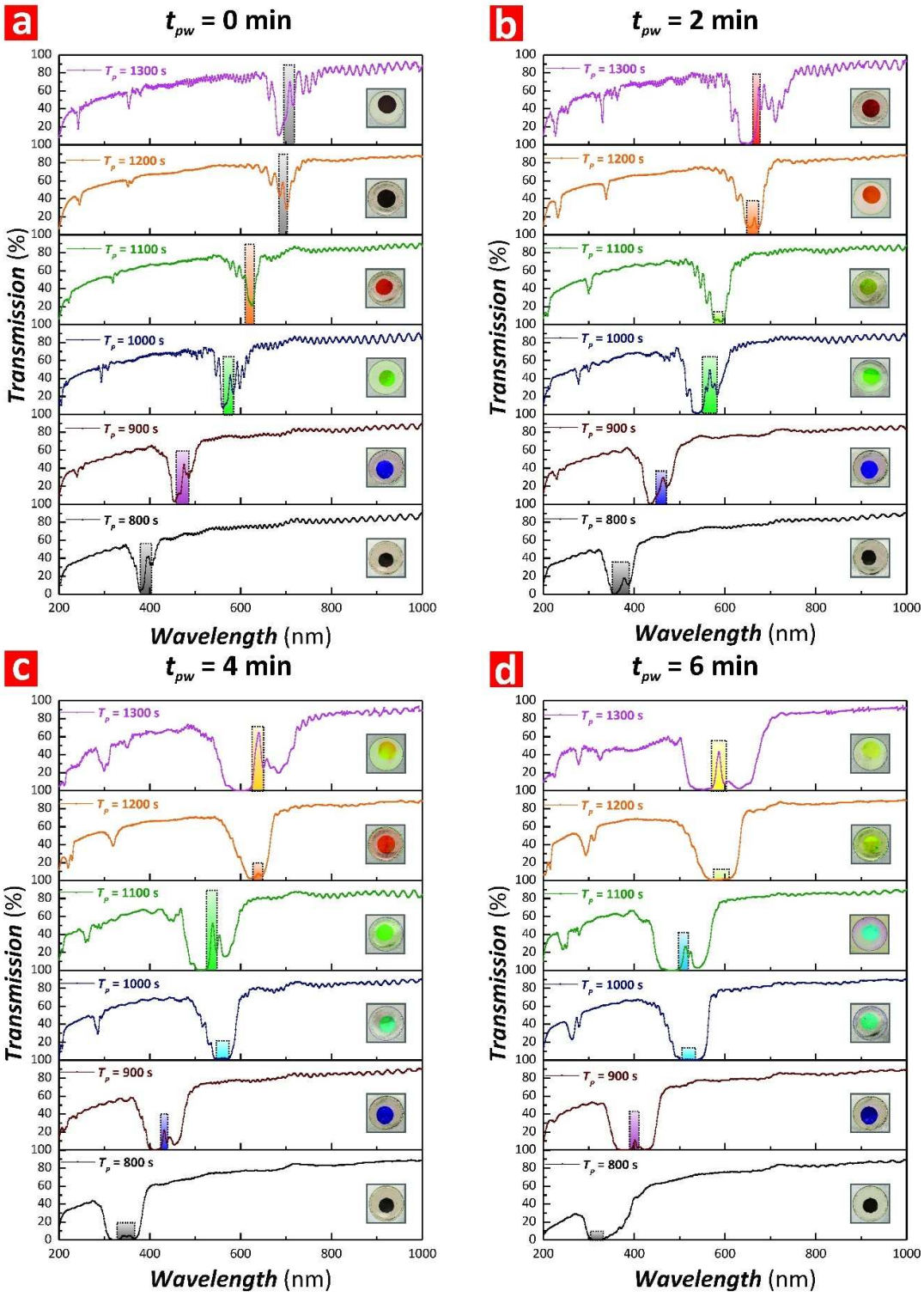

Figure 9. Combinational effect of anodization period (T_P) and pore widening time (t_{pw}) on the optical properties of NAA-μCVs (i.e. quality factor – Q_C, position of resonance band – λ_R, and interferometric color) produced by ASPA. a-d) Transmission spectra showing the position of the resonance band (colored rectangles) and digital pictures (insets) of NAA-μCVs for each anodization period (T_P = 800–1300 s) at different pore widening times (i.e. a) t_{pw} = 0 min, b) t_{pw} = 2 min, c) t_{pw} = 4 min, and d) t_{pw} = 6 min).

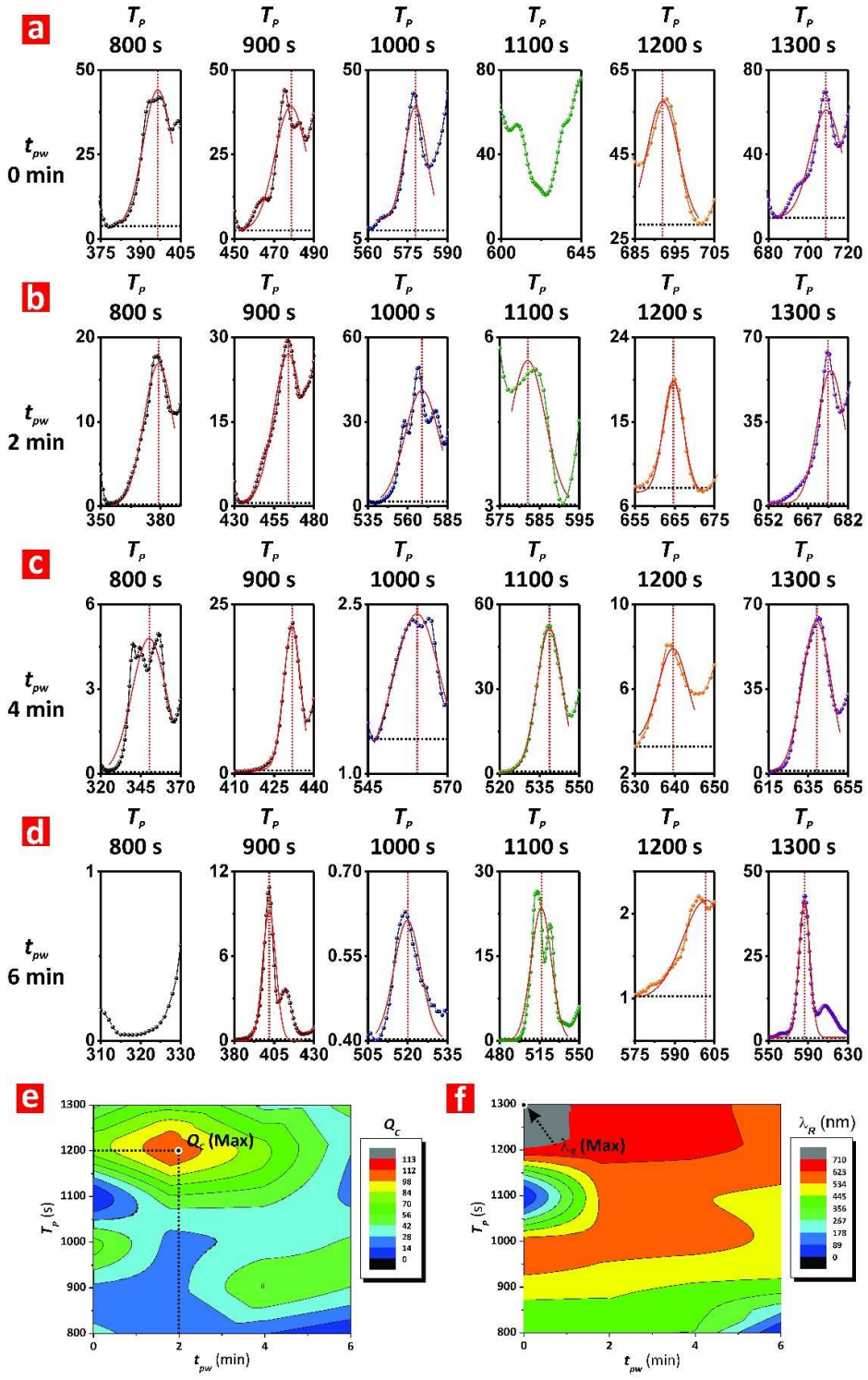

Figure 10. Combinational effect of anodization period (T_P) and pore widening time (t_{pw}) on the resonance band of NAA-μCVs produced by ASPA (note: horizontal dotted black lines denote the baseline (y_0) used for the Gaussian fittings, which correspond to the lower lobe of the PSB, and vertical dotted red lines indicate the central wavelength of the resonance band (λ_R) and the symmetry of the Gaussian fitting). a) t_{pw} = 0 min. b) t_{pw} = 2 min. c) t_{pw} = 4 min. d) t_{pw} = 6 min. e) Contour map showing the dependency of Q_C with T_P and t_{pw} for NAA-μCVs produced with T_P = 800–1300 s. f) Contour map showing the dependency of λ_R with T_P and t_{pw} for NAA-μCVs produced with T_P = 800–1300 s.

Figures 10e and f show contour maps depicting the graphical correlation of Q_C and λ_R of NAA-μCVs with T_P and t_{pw} (**Table S2**). **Figure 10e** reveals that the color fields in the region of shorter T_P (i.e. from 800 to 1000 s) are relatively broad across t_{pw}, from 0 to 6 min, which is a visual indication of the weak correlation of Q_C with the fabrication parameters for NAA-μCVs produced at shorter T_P. Therefore, NAA-μCVs produced at T_P = 800, 900 and 1000 s have low Q_C. In contrast, the color fields become denser with closer field lines when T_P increases from 1100 to 1300 s. This suggests that Q_C has a stronger dependency with longer T_P, where the maximum of Q_C (i.e. 112.6 ± 5.2) is achieved at T_P = 1200 s and t_{pw} = 2 min. The average Q_C estimated for NAA-μCVs as a function of T_P, excluding those PCs without resonance band, was 44.5 ± 23.1. However, seven of these NAA-μCVs showed superior light-confining performance than those reported in previous studies (i.e. Q_C = 56.8 ± 3.2 at T_P = 900 s and t_{pw} = 4 min, Q_C = 60.2 ± 2.1 at T_P = 1000 s and t_{pw} = 0 min, Q_C = 56.5 ± 1.5 at at T_P = 1100 s and t_{pw} = 2 min, Q_C = 75.2 ± 3.3 at T_P = 1200 s and t_{pw} = 0 min, Q_C = 112.6 ± 5.2 at T_P = 1200 s and t_{pw} = 2 min, Q_C = 73.5 ± 4.1 at T_P = 1200 s and t_{pw} = 4 min, and Q_C = 63.1 ± 1.2 at T_P = 1300 s and t_{pw} = 2 min). The distribution of λ_R as a function of T_P and t_{pw} is depicted in **Figure 10f**. This graph shows two local minima in the contour plot due to the absence of resonance bands within the PSB of these NAA-μCVs, which are located at t_{pw} = 0 min for T_P = 1100 s as well as at t_{pw} = 6 min for T_P = 800 s. At t_{pw} = 2 and 4 min, the color distribution reveals a red shift in λ_R resulting from the manipulation of T_P from 800 to 1300 s, where the longest resonance wavelength is achieved at T_P = 1300 s and t_{pw} = 0 min (i.e. 709 ± 1 nm). In general, the longer the anodization period, the longer the wavelength at which NAA-μCVs confine light. This analysis also indicates that an increase in t_{pw} results in a blue shift of λ_R, thus NAA-μCVs confine light of shorter wavelengths although in a less efficient manner as indicated by the Q_C analysis shown in **Figure 10e** due to light scattering effect.

3.4. Effect of Current Density Offset (J_{offset}) on the Optical Properties of Nanoporous Anodic Alumina Microcavities. To further understand the effect of the different fabrication parameters on the photonic features of NAA-μCVs produced by ASPA, we investigated the how the current density offset (J_{offset}) affects the quality factor and the tuning of resonance bands of NAA-μCVs. To this end, J_{offset} was systematically modified from 0.140 to 0.560 mA cm^{-2} with an interval of 0.140 mA cm^{-2} while keeping constant the rest of fabrication parameters (i.e. T_P = 1300 s, J_{offset} = 0.280 mA cm^{-2}, and ΔA_J = 0.210 mA cm^{-2}). The anodization profiles of NAA-μCVs produced at different J_{offset} are compiled in **Figure S4 (Supporting Information)**. The transmission spectra of these NAA-μCVs shown in **Figures 11a-d** were analyzed to establish the effect of this fabrication parameter on Q_C and λ_R. **Figure 11a** shows the transmission spectra of NAA-μCVs produced at J_{offset} = 0.140 mA cm^{-2} as a function of t_{pw} (i.e. 0 to 6 min). The PSB of this set of NAA-μCVs is located within the visible region, with a very weak resonance band that is almost vanished at long pore widening times (i.e. t_{pw} > 2 min). The pore widening treatment blue-shifts the position of the PSB and leads the NAA-μCV to lose its light-confining characteristics. The transmission spectra shown in **Figure 11b** reveals that the position of the PSB of NAA-μCVs produced at J_{offset} = 0.280 mA cm^{-2} are located within the upper range of visible spectrum (i.e. 600–800 nm). Unlike NAA-μCVs produced at J_{offset} = 0.140 mA cm^{-2}, the resonance band of these NAA-μCVs (J_{offset} = 0.280 mA cm^{-2}) remains well-resolved and sharp after pore widening from 0 to 6 min. On the other hand, both sets of NAA-μCVs produced at J_{offset} = 0.420 and 0.560 mA cm^{-2} have their PSBs located in the NIR range (i.e. 900–1100 nm) (**Figures 11c and d**). These NAA-μCVs also show the presence of an intense resonance band within their PSB, which is slightly widen and blue-shifted with the pore widening treatment, from 0 to 6 min.

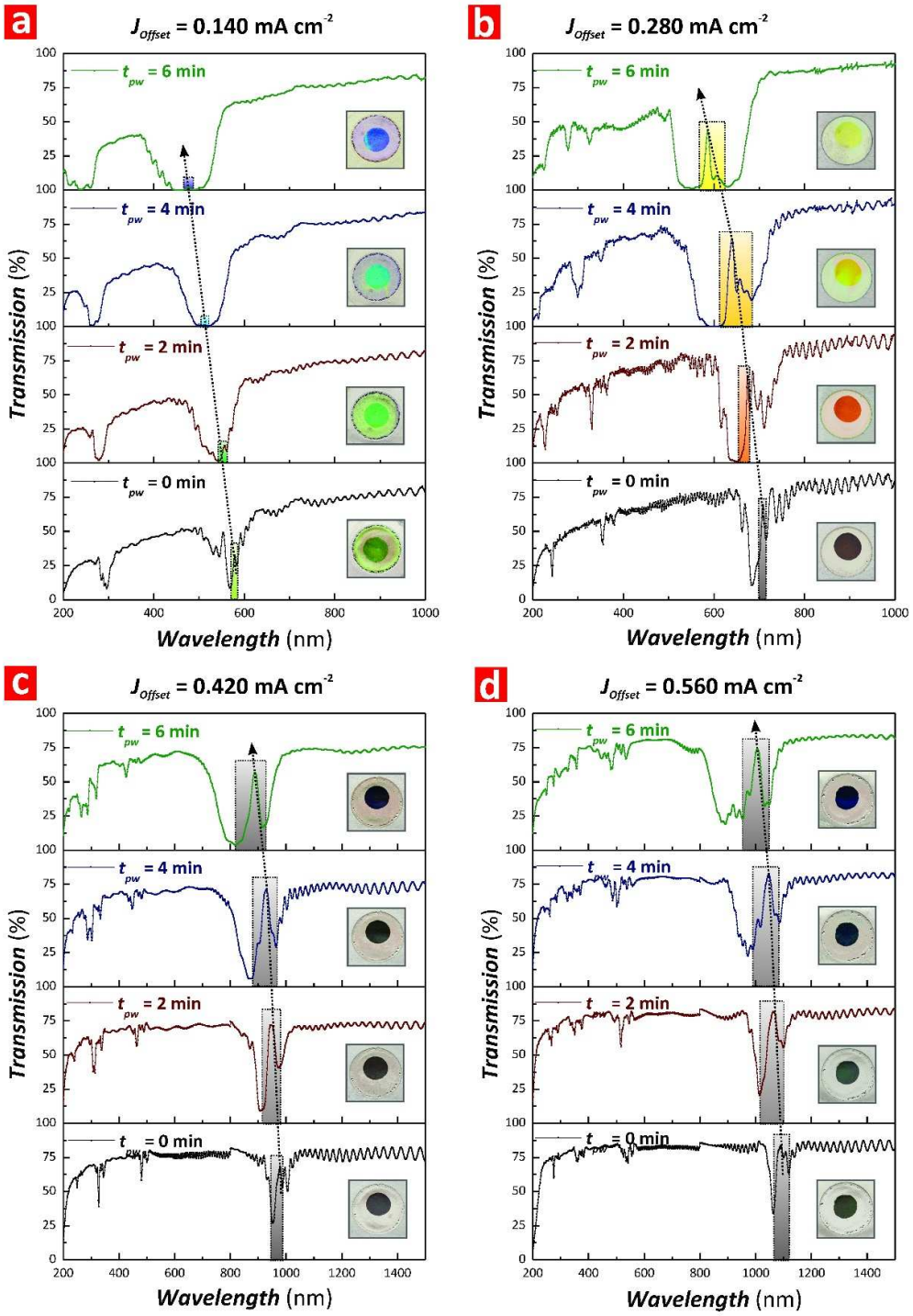

Figure 11. Combinational effect of anodization offset (J_{Offset}) and pore widening time (t_{pw}) on the optical properties of NAA-μCVs (i.e. quality factor – Q_C, position of resonance band – λ_R, and interferometric color) produced by ASPA. a-d) Transmission spectra showing the position of the resonance band, digital pictures (insets) of NAA-μCVs for each anodization offset (J_{Offset} = 0.140–0.560 mA cm^{-2}) at different pore widening times (from 0 to 6 min) (i.e. a) J_{Offset} = 0.140 mA cm^{-2}, b) J_{Offset} = 0.280 mA cm^{-2}, c) J_{Offset} = 0.420 mA cm^{-2}, and d) J_{Offset} = 0.560 mA cm^{-2}) (note: color rectangles denote the approximate position of the resonance band within the PSB and black dotted arrow lines indicate the blue shift of the resonance bands with t_{pw}).

By comparing the transmission spectra at different J_{offset}, it is apparent that an increase in J_{offset} causes a red shift in the position of resonance band. As the digital images shown in the insets in **Figures 11a-d** demonstrate, these NAA-μCVs display vivid interferometric colors, which are affected by the fabrication parameters: J_{offset} and t_{pw}. Although these NAA-μCVs show second and third order PSBs, the color displayed by these PCs corresponds to the wavelength at which the first order PSB is located, denoting a more efficient reflection of light within these spectral regions. In this case, NAA-μCVs produced at lower J_{offset} (i.e. 0.140 and 0.280 mA cm^{-2}) display vivid colors corresponding to the position of their PSB in the visible spectral range. In contrast, the PSBs of NAA-μCVs produced with high J_{offset} (i.e. 0.420 and 0.560 mA cm^{-2}) are within the NIR range, thus no color is observed (i.e. transparent – black). **Figures 12a-d** show magnified views of the resonance bands and Gaussian fittings used to estimate λ_R, $FWHM_R$ and Q_C for these NAA-μCVs and **Figures 12e and f** compile a summary of the estimated values for Q_C and λ_R in the form of contour maps. The visual analysis of the magnified resonance bands shown in **Figures 12a-d** reveals that, in general, the intensity of the resonance band increases with J_{Offset} and decreases with t_{pw}. A closer analysis of the values of Q_C, visually shown in **Figure 12e** and compiled in **Table S3 (Supporting Information)**, reveals that the combination of low values of J_{offset} (e.g. 0.140-0.280 mA cm^{-2}) and moderate pore widening times (i.e. 2-4 min) are favorable in the production of NAA-μCVs with high quality resonance bands. The Q_C maximum is achieved by NAA-μCVs produced with J_{offset} = 0.140 mA cm^{-2} and t_{pw} = 4 min (i.e. 65.5 ± 2.3), although these PC structure show considerably weaker resonance bands as compared to their counterparts produced at higher J_{Offset} (i.e. > 0.140 mA cm^{-2}). The dependency of Q_C on J_{offset} increases within the range 0.140-0.420 mA cm^{-2}, as denoted by the denser color fields with short distance between adjacent field lines.

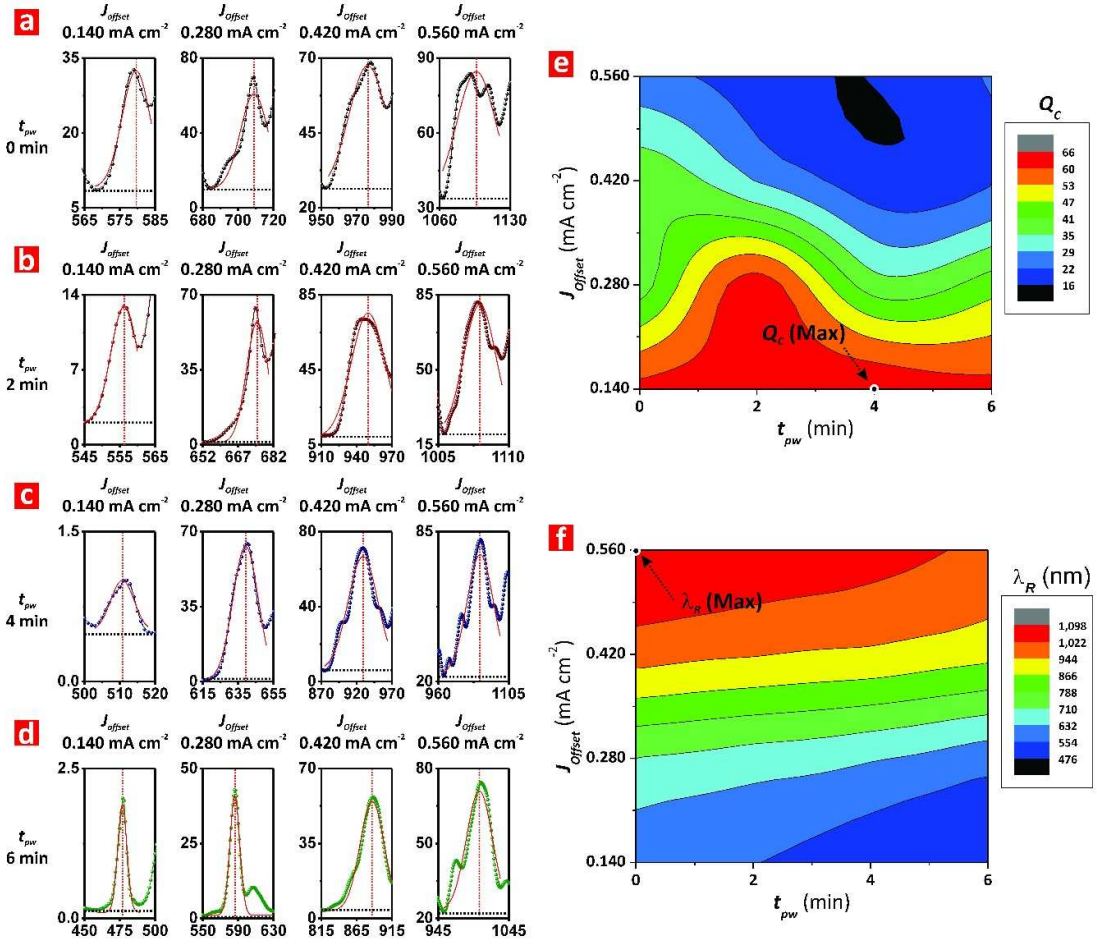

Figure 12. Combinational effect of current density offset (J_{Offset}) and pore widening time (t_{pw}) on the resonance band of NAA-μCVs produced by ASPA (note: horizontal dotted black lines denote the baseline (y_0) used for the Gaussian fittings, which correspond to the lower lobe of the PSB, and vertical dotted red lines indicate the central wavelength of the resonance band (λ_R) and the symmetry of the Gaussian fitting). a) J_{Offset} = 0.140 mA cm^{-2}, b) J_{Offset} = 0.280 mA cm^{-2}, c) J_{Offset} = 0.420 mA cm^{-2}, and d) J_{Offset} = 0.560 mA cm^{-2}. e) Contour map showing the dependency of Q_C with J_{Offset} and t_{pw} for NAA-μCVs produced with J_{Offset} = 0.140–0.560 mA cm^{-2}. f) Contour map showing the dependency of λ_R with J_{Offset} and t_{pw} for NAA-μCVs produced with J_{Offset} = 0.140–0.560 mA cm^{-2}.

The broad color fields and more separated field lines at the region of high J_{offset} and long t_{pw} suggest a weak dependency of Q_C with these combinations of fabrication parameters, which worsens the quality of the microcavity structure. The average Q_C estimated for NAA-μCVs as a function of J_{Offset} was 39.1 ± 18.4 and five of these NAA-μCVs showed slightly superior light-confining performance than those reported in previous studies (i.e. Q_C = 61.7 ± 2.2 at J_{Offset} = 0.140 mA cm^{-2} and t_{pw} = 0 min, Q_C = 62.5 ± 3.4 at J_{Offset} = 0.140 mA cm^{-2} and t_{pw} = 2 min, Q_C = 65.5 ± 3.6 at J_{Offset} = 0.140 mA cm^{-2} and t_{pw} = 4 min, Q_C = 61.9 ± 2.4 at J_{Offset} =

0.140 mA cm^{-2} and t_{pw} = 6 min, and Q_C = 63.1 ± 1.2 at J_{Offset} = 0.280 mA cm^{-2} and t_{pw} = 2 min). The effect of J_{offset} and t_{pw} on the position of the resonance band of NAA-μCVs is summarized in the contour map shown in **Figure 12f**. This contour map shows that the field line distances at low J_{offset} (i.e. J_{offset} < 0.280 mA cm^{-2}) and high J_{offset} (i.e. J_{offset} > 0.420 mA cm^{-2}) are relatively wide. However, the color fields become closer with shorter equidistant field lines for J_{offset} between 0.280 and 0.420 mA cm^{-2}, which indicates a stronger dependency of λ_R with J_{offset} within that range of fabrication parameters. It is verified that λ_R is red-shifted towards the NIR region by increasing J_{offset}. The higher J_{offset} is, the longer the wavelength at which light is confined within the structure of NAA-μCVs produced by ASPA. The maximum value of λ_R (i.e. 1096 ± 1 nm) is located at J_{offset} = 0.560 mA cm^{-2} and t_{pw} = 0 min. An increase in t_{pw} has an opposite effect to that of J_{offset} on the shifting of λ_R. However, J_{offset} has a more significant effect on the position of the resonance band as denoted by the color field distribution.

CONCLUSIONS

In summary, this study has demonstrated that a rational design of the nanoporous structure of NAA-based optical microcavities using apodized stepwise pulse anodization can lead to an enhancement of the light-confining capabilities of these PCs. The structure of these optical microcavities is composed of two apodized NAA-DBRs, which can confine light efficiently (i.e. Q_C = 112.6 ± 5.2). Furthermore, this nanofabrication approach enables the fine-tuning of the optical properties of the two highly reflective mirrors so light can be confined within the PC structure more efficiently across the spectral regions. The optical properties of NAA-based optical microcavities were assessed in terms of quality factor, position of resonance band, and interferometric colors. The anodization parameters investigated were anodization period, anodization time, current density offset and pore

widening time. A systematic modification of these parameters allowed to establish optimization paths toward more efficient light-confining NAA-based PC structures.

In general, our study established that a combination of longer anodization time, longer anodization period, short pore widening time, and moderate current density offset generates optical microcavities with high quality factor, where the most optimal NAA-μCV was that produced with 20 h anodization time, 1200 s anodization period, 2 min of pore widening, and 0.280 mA cm^{-2} of current density offset. Our results provide a better understanding and solid foundation to further enhance the light-confining capabilities of NAA-based optical microcavities, opening new opportunities for further fundamental and applied research for these nanoporous PC structures in optical sensing, photonics, and optoelectronics.

Supporting Information

The Supporting Information file provides information about the structure of NAA-μCVs at different pore widening times, anodization profiles of NAA-μCVs produced by ASPA at different anodization periods, from 800 to 1300 s, and current density offsets, from 0.140 to 0.560 mA cm^{-2}, and a compilation of the values of y_0, λ_R, $FWHM_R$, Q_C, and R^2.

Author Information

Doctor Abel Santos
Research for Impact Fellow – Lecturer
School of Chemical Engineering – The University of Adelaide
Phone: +61 8 8313 1535
Email: abel.santos@adelaide.edu.au
Web page: http://www.adelaide.edu.au/directory/abel.santos
Professor Andrew Abell
Professor of Chemistry and node director of the ARC Centre of Excellence for Nanoscale Biophotonics
School of Chemistry and Physics – The University of Adelaide
Phone: + 61 8 8313 5652

Email: andrew.abell@adelaide.edu.au

Web page: http://researchers.adelaide.edu.au/profile/andrew.abell#contact-details

Acknowledgements

Authors thank the support provided by the Australian Research Council (ARC) through the grants number DE140100549 and CE140100003, the School of Chemical Engineering, the University of Adelaide (DVCR initiative 'Research for Impact'), the Institute for Photonics and Advanced Sensing (IPAS), and the ARC Centre of Excellence for Nanoscale BioPhotonics (CNBP).

REFERENCES

1 Michler, P.; Kiraz, A.; Becher, C.; Schoenfeld, W.; Petroff, P.; Zhang, L.; Hu, E.; Imamoglu, A. A quantum dot single-photon turnstile device. *Science* **2000**, *290*, 2282-2285.

2 Ogawa, S.; Imada, M.; Yoshimoto, S.; Okano, M.; Noda, S. Control of light emission by 3D photonic crystals. *Science* **2004**, *305*, 227-229.

3 Noda, S.; Chutinan, A.; Imada, M. Trapping and emission of photons by a single defect in a photonic bandgap structure. *Nature* **2000**, *407*, 608-610.

4 Song, B.-S.; Asano, T.; Noda, S. Physical origin of the small modal volume of ultra-high-Q photonic double-heterostructure nanocavities. *New J. Phys.* **2006**, *8*, 209.

5 Notomi, M. Manipulating light with strongly modulated photonic crystals. *Rep. Prog. Phys.* **2010**, *73*, 096501.

6 Lee, H.; Chen, T.; Li, J.; Yang, K.Y.; Jeon, S.; Painter, O.; Vahala, K.J. Chemically etched ultrahigh-Q wedge-resonator on a silicon chip. *Nat. Photonics* **2012**, *6*, 369-373.

7 Vahala, K.J. Optical microcavities. *Nature* **2003**, *424*, 839-846.

8 Matsko, A. B. *Practical applications of microresonators in optics and photonics*. Boca Raton: CRC Press, 2009.

9 Yablonovitch, E. Inhibited spontaneous emission in solid-state physics and electronics. *Phys. Rev. Lett.* **1987**, *58*, 2059.

10 John, S. Strong localization of photons in certain disordered dielectric superlattices. *Phys. Rev. Lett.*, 1987, **58,** 2486.

11 Krauss, T.F. Photonic crystals: Cavities without leaks. *Nature Mater.* **2003**, *2*, 777-778.

12 Foresi, J.; Villeneuve, P.R.; Ferrera, J.; Thoen, E.; Steinmeyer, G.; Fan, S.; Joannopoulos, J.; Kimerling, L.; Smith, H. I.; Ippen, E. Photonic-bandgap microcavities in optical waveguides. *Nature* **1997**, *390*, 143-145.

13 Sun, H.-B.; Mizeikis, V.; Xu, Y.; Juodkazis, S.; Ye, J.-Y.; Matsuo, S.; Misawa, H. Microcavities in polymeric photonic crystals. *Appl. Phys. Lett.* **2001**, *79*, 1-3.

14 Ripin, D.J.; Lim, K.-Y.; Petrich, G.; Villeneuve, P.R.; Fan, S.; Thoen, E.; Joannopoulos, J. D.; Ippen, E.; Kolodziejski, L. One-dimensional photonic bandgap microcavities for strong optical confinement in GaAs and GaAs/AlxOy semiconductor waveguides. *J. Lightwave Technol.* **1999**, *17*, 2152.

15 Baba, T. Photonic crystals and microdisk cavities based on GaInAsP-InP system. *IEEE J. Sel. Top. Quantum Electron.* **1997**, *3*, 808-830.

16 Solomon, G.; Pelton, M.; Yamamoto, Y. Single-mode spontaneous emission from a single quantum dot in a three-dimensional microcavity. *Phys. Rev. Lett.* **2001**, *86*, 3903.

17 Benson, T.M.; Boriskina, S.V.; Sewell, P.; Vukovic, A.; Greedy, S.C.; Nosich, A.I. Micro-optical resonators for microlasers and integrated optoelectronics. In *Frontiers in planar lightwave circuit technology*, Springer: 2006; pp 39-70.

18 Zain, A.R.M.; Johnson, N.P.; Sorel, M.; Richard, M. Ultra high quality factor one dimensional photonic crystal/photonic wire micro-cavities in silicon-on-insulator (SOI). *Opt. Express* **2008**, *16*, 12084-12089.

19 Akahane, Y.; Asano, T.; Song, B.-S.; Noda, S. High-Q photonic nanocavity in a two-dimensional photonic crystal. *Nature* **2003**, *425*, 944-947.

20 Pavesi, L.; Mazzoleni, C.; Tredicucci, A.; Pellegrini, V. Controlled photon emission in porous silicon microcavities. *Appl. Phys. Lett.* **1995**, *67*, 3280-3282.

21 Pellegrini, V.; Tredicucci, A.; Mazzoleni, C.; Pavesi, L. Enhanced optical properties in porous silicon microcavities. *Phys. Rev. B* **1995**, *52*, R14328.

22 Cazzanelli, M.; Pavesi, L. Time-resolved photoluminescence of all-porous-silicon microcavities. *Phys. Rev. B* **1997**, *56*, 15264.

23 Ghulinyan, M.; Oton, C.; Bonetti, G.; Gaburro, Z.; Pavesi, L. Free-standing porous silicon single and multiple optical cavities. *J. Appl. Phys.* **2003**, *93*, 9724-9729.

24 Pavesi, L.; Panzarini, G.; Andreani, L. All-porous silicon-coupled microcavities: Experiment versus theory. *Phys. Rev. B* **1998**, *58*, 15794.

25 De Stefano, L.; Moretti, L.; Rendina, I.; Rossi, A. M. Porous silicon microcavities for optical hydrocarbons detection. *Sens. Actuators, A* **2003**, *104*, 179-182.

26 Mulloni, V.; Pavesi, L. Porous silicon microcavities as optical chemical sensors. *Appl. Phys. Lett.* **2000**, *76*, 2523-2525.

27 Reece, P.; Lérondel, G.; Zheng, W.; Gal, M. Optical microcavities with subnanometer linewidths based on porous silicon. *Appl. Phys. Lett.* **2002**, *81*, 4895-4897.

28 Lehmann, V. *Electrochemistry of Silicon: Instrumentation, Science, Materials and Applications*. Wiley: 2002.

29 Chen, Y.; Santos, A.; Wang, Y.; Kumeria, T.; Li, J.; Wang, C.; Losic, D. Biomimetic nanoporous anodic alumina distributed bragg reflectors in the form of films and microsized particles for sensing applications. *ACS Appl. Mater. Interfaces* **2015**, *7*, 19816-19824.

30 Yu, M.; Li, C.; Yang, Y.; Xu, S.; Zhang, K.; Cui, H.; Zhu, X. Cavities between the double walls of nanotubes: Evidence of oxygen evolution beneath an anion-contaminated layer. *Electrochem. Commun.* **2018**, *90*, 34-38.

31 Yu, M.; Chen, Y.; Li, C.; Yan, S.; Cui, H.; Zhu, X.; Kong, J. Studies of oxide growth location on anodization of Al and Ti provide evidence against the field-assisted dissolution and field-assisted ejection theories. *Electrochem. Commun.* **2018**, *87*, 76-80.

32 Yu, M.; Cui, H.; Ai, F.; Jiang, L.; Kong, J.; Zhu, X. Terminated nanotubes: Evidence against the dissolution equilibrium theory. *Electrochem. Commun.* **2018**, *86*, 80-84.

33 Zhao, S.; Xing, J.; Fan, H.; Zhang, S.; Li, D.; Zhu, X. Derivation of a mathematical model for the growth of anodic TiO_2 nanotubes under constant current conditions. *J. Electrochem. Soc.* **2017**, *164*, E187-E193.

34 Wen, L.; Xu, R.; Mi, Y.; Lei, Y. Multiple nanostructures based on anodized aluminium oxide templates. *Nat. Nanotechnol.* **2017**, *12*, 244-250.

35 Xu, R.; Wen, L.; Wang, Z.; Zhao, H.; Xu, S.; Mi, Y.; Xu, Y.; Sommerfeld, M.; Fang, Y.; Lei, Y. Three-dimensional plasmonic nanostructures design for boosting photoelectrochemical activity. *ACS Nano* **2017**, *11*, 7382-7389.

36 Zhan, Z.; Xu, R.; Mi, Y.; Zhao, H.; Lei, Y. Highly controllable surface plasmon resonance property by heights of ordered nanoparticle arrays fabricated via a nonlithographic route. *ACS Nano* **2015**, *9*, 4583-4590.

37 Lee, J.; Bae, K.; Kang, G.; Choi, M.; Baek, S.; Yoo, D.-S.; Lee, C.-W.; Kim, K. Graded-lattice AAO photonic crystal heterostructure for high *Q* refractive index sensing. *RSC Adv.* **2015**, *5*, 71770-71777.

38 Wang, Y.; Chen, Y.; Kumeria, T.; Ding, F.; Evdokiou, A.; Losic, D.; Santos, A. Facile synthesis of optical microcavities by a rationally designed anodization approach: tailoring photonic signals by nanopore structure. *ACS Appl. Mater. Interfaces* **2015**, *7*, 9879-9888.

39 Shang, G. L.; Fei, G. T.; De Zhang, L. Experimental realization of tunable defect mode in photonic crystal. *J. Phys. D: Appl. Phys.* **2015**, *48*, 435304.

40 Lee, W.; Schwirn, K.; Steinhart, M.; Pippel, E.; Scholz, R.; Gösele, U. Structural engineering of nanoporous anodic aluminium oxide by pulse anodization of aluminium. *Nat. Nanotechnol.* **2008**, *3*, 234-239.

41 Yan, P.; Fei, G.-T.; Li, H.; Shang, G.-L.; Wu, B.; Zhang, L.-D. Alumina photonic crystals with defect modes for sensor application. Chin. J. Chem. Phys. 2014, 27, 121-124.

42 Ghulinyan, M.; Oton, C.J.; Bonetti, G.; Gaburro, Z.; Pavesi, L. Free-standing porous silicon single and multiple optical cavities. *J. Appl. Phys.*, **2003**, *93*, 9724-9729.

43 Reece, P.J.; Lérondel, G.; Zheng, W.H.; Gal, M. Optical microcavities with subnanometer linewidths based on porous silicon. *Appl. Phys. Lett.*, **2002**, *81*, 4895-4897.

44 Lee, W.; Scholz, R.; Gösele, U. A continuous process for structurally well-defined Al2O3 nanotubes based on pulse anodization of aluminum. *Nano Lett.* **2008**, *8*, 2155-2160.

45 Lee, W.; Kim, J.-C. Highly ordered porous alumina with tailor-made pore structures fabricated by pulse anodization. *Nanotechnology* **2010**, *21*, 485304.

46 Lee, W.; Ji, R.; Gösele, U.; Nielsch, K. Fast fabrication of long-range ordered porous alumina membranes by hard anodization. *Nature Mater.* **2006**, *5*, 741-747.

47 Santos, A. Nanoporous anodic alumina photonic crystals: Fundamentals, developments and perspectives. *J. Mater. Chem. C* **2017**, *5*, 5581-5599

48 Chen, Y.; Santos, A.; Ho, D.; Wang, Y.; Kumeria, T.; Li, J.; Wang, C.; Losic, D. On the generation of interferometric colors in high purity and technical grade aluminum: An alternative green process for metal finishing industry. *Electrochim. Acta* **2015**, *174*, 672-681.

49 Macias, G.; Ferré-Borrull, J.; Pallarès, J.; Marsal, L.F. 1-D nanoporous anodic alumina rugate filters by means of small current variations for real-time sensing applications. *Nanoscale Res. Lett.* **2014**, *9*, 315.

50 Zheng, W.J.; Fei, G.T.; Wang, B.; Jin, Z.; Zhang, L.D. Distributed Bragg reflector made of anodic alumina membrane. *Mater. Lett.* **2009**, *63*, 706-708.

51 Shang, G.L.; Fei, G.T.; Zhang, Y.; Yan, P.; Xu, S.H.; Zhang, L.D. Preparation of narrow photonic bandgaps located in the near infrared region and their applications in ethanol gas sensing. *J. Mater. Chem. C* **2013**, *1*, 5285-5291.

52 Law, C.S.; Santos, A.; Nemati, M.; Losic, D. Structural engineering of nanoporous anodic alumina photonic crystals by sawtooth-like pulse anodization. *ACS Appl. Mater. Interfaces* **2016**, *8*, 13542-13554.

53 Nemati, M.; Santos, A.; Law, C. S.; Losic, D. Assessment of binding affinity between drugs and human serum albumin using nanoporous anodic alumina photonic crystals. *Anal. Chem.* **2016**, *88*, 5971-5980.

54 Santos, A.; Law, C.S.; Lei, D.W.C.; Pereira, T.; Losic, D. Fine tuning of optical signals in nanoporous anodic alumina photonic crystals by apodized sinusoidal pulse anodisation. *Nanoscale* **2016**, *8*, 18360-18375.

55 Santos, A.; Pereira, T.; Law, C.S.; Losic, D. Rational engineering of nanoporous anodic alumina optical bandpass filters. *Nanoscale* **2016**, *8*, 14846-14857.

56 Santos, A.; Law, C.S.; Pereira, T.; Losic, D. Nanoporous hard data: optical encoding of information within nanoporous anodic alumina photonic crystals. *Nanoscale* **2016**, *8*, 8091-8100.

57 Nemati, M.; Santos, A.; Kumeria, T.; Losic, D. Label-free real-time quantification of enzyme levels by interferometric spectroscopy combined with gelatin-modified nanoporous anodic alumina photonic films. *Anal. Chem.* **2015**, *87*, 9016-9024.

58 Chen, Y.; Santos, A.; Wang, Y.; Kumeria, T.; Ho, D.; Li, J.; Wang, C.; Losic, D. Rational design of photonic dust from nanoporous anodic alumina films: a versatile photonic nanotool for visual sensing. *Sci. Rep.* **2015**, *5*, 12893.

59 Kumeria, T.; Rahman, M.M.; Santos, A.; Ferré-Borrull, J.; Marsal, L.F.; Losic, D. Nanoporous anodic alumina rugate filters for sensing of ionic mercury: Toward environmental point-of-analysis systems. *ACS Appl. Mater. Interfaces* **2014**, *6*, 12971-12978.

60 Law, C. S.; Lim, S. Y.; Santos, A. On the precise tuning of optical filtering features in nanoporous anodic alumina distributed Bragg reflectors. *Sci. Rep.* **2018**, *8*, 4642.

61 Southwell, W. H. Using apodization functions to reduce sidelobes in rugate filters. *Appl. Opt.* **1989**, *28*, 5091-5094.

62 Asano, T.; Song, B.-S.; Noda, S. Analysis of the experimental Q factors (~ 1 million) of photonic crystal nanocavities. *Opt.* Express **2006**, *14*, 1996-2002.

63 Abràmoff, M.D.; Magalhaes, P.J.; Ram, S.J. Image processing with ImageJ. *Biophotonics Int.*, **2004**, *11*, 36-42.

64 Jalkanen, T.; Mäkilä, E.; Suzuki, Y. I.; Urata, T.; Fukami, K.; Sakka, T.; Salonen, J.; Ogata, Y. Studies on chemical modification of porous silicon-based graded-index optical microcavities for improved stability under alkaline conditions. *Adv. Funct. Mater.* **2012**, *22*, 3890-3898.

65 Jenie, S.A.; Pace, S.; Sciacca, B.; Brooks, R.D.; Plush, S.E.; Voelcker, N.H. Lanthanide luminescence enhancements in porous silicon resonant microcavities. *ACS Appl. Mater. Interfaces* **2014**, *6*, 12012-12021.

TABLE OF CONTENTS